FACULTY OF SCIENCE AND TECHNOLOGY

MASTER THESIS

Study programme / specialisation: Master of Science Structural and Mechanical Engineering	The spring semester, 2022 Open
Author: Sindre Tronsli	Sindre Tronsli (signature author)
Course coordinator: Sudath C. Siriwardane Supervisor(s): Yanyan Sha	
Thesis title: A study on ship-bridge collisions and the significance of the collision energy and impact angle for the probability of collapse	
Credits (ECTS): 30	
Keywords: Ship-collision Heinrich Factor FEA LS-Dyna Simulations	Pages: 72 + appendix: 13 Stavanger, 15th June/2022 date/year

Abstract

Bridges are a necessity for transportation across waterways in modern society, and the passing of large ships below bridges poses the risk of ship-bridge collision, which can, in the worst case, lead to the total collapse of the bridge with fatalities and high economic costs. Ship-bridge collisions have been studied extensively over the past years to understand and reduce these risks.

This thesis study how different impact conditions related to the impact velocity, ship mass, and impact angle affect the collision and the probability of collapse. It includes numerous simulations using different impact conditions and proposes models that relate the impact conditions and collision response to the likelihood of collapse, modelled as the Heinrich Factor.

The first step was to get to familiar with the finite element software LS-Dyna through an introductory course and self-studies. The finite element model of the bridge structure was created in LS-Dyna, and ship-bridge collision simulations with different impact conditions were performed. The simulation results were analysed and used to determine the probability of collapse of the bridge pier. Additionally, two scripts in Python were developed to apply machine learning principles to predict the collapse of a bridge pier, using the simulation results as data.

Preface and Acknowledgements

This study was conducted in the spring of 2022 and marked the end of the master programme, Master of Science in Structural and Mechanical Engineering at the University of Stavanger. The scope of the work included getting familiar with the FE software LS-Dyna, building a finite element bridge model in LS-Dyna, and analysing numerous ship-bridge collision simulations to propose methods for determining the Heinrich Factor for the particular bridge model.

First, I want to thank my supervisor, Professor Yanyan Sha, UiS. He provided insightful and valuable knowledge about ship-bridge collisions and had several interesting theories and thoughts about the subject. I also want to thank DYNAmore and my contact person in DYNAmore, Klas Engstrand, who arranged a very insightful introductory course in LS-Dyna and helped with technical questions about LS-Dyna. Lastly, I want to thank my friends Sander and Soban for assisting me with the language and the development of the machine learning scripts. The help from everyone mentioned above really raised the quality of the thesis, and the thesis would not be possible without them.

Table of Contents

Figures and Tables

List of Abbreviations

AASHTO	The American Association of State Highway and Transportation Officials
ALARP	As low as Reasonably Practicable
API	American Petroleum Institute
DOF	Degree(s) of Freedom
DR	Drift Ratio
FE	Finite Element
FEA	Finite Element Analysis
KE	Kinetic Energy
LSTC	Livermore Software Technology Corporation
t	Metric Tonnes

List of Symbols

p	Momentum
m	Mass
v	Velocity
F	Force
t	Time
a	Acceleration
I	Impulse
E_k	KE
Δt	Time-step increment
Δt_{cr}	Critical time-step
ω	Angular frequency
ω_d	Damped angular frequency
T	Natural period
ξ	Damping ratio
C	Damping coefficient
C_c	Critical damping coefficient
ε	Strain

1. Introduction

Bridges above sea or inland waterways are vulnerable to ship collision, and ship-bridge collisions can result in casualties and massive economic consequences. With the increase in shipping traffic and vessel size, these risks increase, and managing the risk of ship-bridge collisions becomes even more important (Larsen, 1993). Thus, it is essential to study ship-bridge collisions and design bridges that can withstand impacts from ships to reduce the risk of ship-bridge collisions.

Statistically, at least one serious ship collision accident occurs per year globally, and there have been 34 major bridge collapses, with a total loss of 346 lives between 1960 and 2007 (Sha & Hao, 2012). Some examples of severe ship-bridge collisions are the collision between a barge and a twin-girder bridge in Oklahoma, USA, in 2002, with 13 fatalities, and the collision between a cargo vessel and the Jiujiang cable-stayed bridge in Guangdong, China, in 2007, with eight casualties. In addition to fatalities, ship-bridge collisions will have severe economic and social consequences, including the disruption of critical infrastructure for private transportation and emergency units and the possibility of environmental damage due to oil and chemical spills. (Knott & Winters, 2018).

The study focuses on the probability of collapse of the bridge in the event of a ship collision incident with a ship capable of causing critical failure. This probability can be modelled as the Heinrich Factor (Zhang et al., 2019c, p. 45). However, the procedure for determining the Heinrich Factor is not clearly defined for bridge-ship collision. The study will define the Heinrich Factor for ship-bridge collisions and establish relationships between the Heinrich Factor and important collision characteristics like impact velocity, ship mass, and impact angle. A simplified FE model of a bridge is created, and a FEA, including numerous ship-bridge simulations, is performed, and the simulation results are analysed to establish a relationship between the different collision characteristics and the Heinrich Factor.

2. Literature Review

Because of the increase in shipping traffic and vessel size (Tran & Haasis, 2015) and past catastrophic ship collision events, ship collision is important to study and understand. In 1958, Minorsky conducted the first significant study of ship collision. He performed 26 ship-ship collision tests and proposed empirical formulas for penetration resistance and absorbed energy. (Minorsky, 1958). Woisin (1976) conducted further experimental testing and modified the empirical formulas presented by Minorsky. The experimental studies conducted by Minorsky and Woisin provided essential knowledge and data about ship-ship collisions and the collision process in general.

In 1980, the Sunshine Skyway Bridge in the USA collapsed due to a ship collision (Garder, 2017). This catastrophic event increased the awareness of vessel-bridge collision and bridge collapse due to vessel collision and acted as a starting point for studies on vessel-bridge collision (AASHTO, 2009). The American Association of State Highway and Transportation Officials (AASHTO) began the development of design codes for bridges and vessel collisions in 1988. The design code 'Guide Specifications and Commentary for Vessel Collision Design of Highway Bridges' was released in 1991 and was later updated in 2009 (AASHTO, 2009).

The design code provides design provisions for bridges susceptible to ship collision. The purpose was to minimise the bridge's susceptibility to damage in the case of ship collision (AASHTO, 2009). The AASHTO guideline deploys a static analysis procedure and provides a simple and useful guideline for bridge design for ship collisions. However, as the guideline deploys a static analysis, it neglects the dynamic effects and material nonlinearities that can considerably affect the impact load and bridge response (Sha & Hao, 2014).

Consolazio et al. (2006) performed experimental barge-bridge collision tests and proposed numerical models to estimate barge impact loads with dynamic effects. However, performing realistic ship-bridge collision tests are expensive and time-consuming. Therefore, the FE method is preferred for conducting ship-bridge collision studies with dynamic effects and has proven to produce reliable results (Pedersen et al., 1993).

Consolazion and Cowan (2003) used the FE code ADINA to develop numerical models and analyse the impact forces of barge collisions against bridge piers. Yuan and Harik (2008) used the FE software LS-Dyna to create 3D numerical models and study the time histories for impact loads for different pier geometries. Sha and Hao (2013), (2014) developed 3d FE models of reinforced bridge piers to consider the nonlinear pier responses in a ship-bridge collision. They

studied the nonlinear pier responses by simulating barge-pier collisions, and proposed empirical formulas to determine the dynamic barge impact force using the same models. Fan and Yuan (2014) deployed FE-based techniques and analytical methods to determine the ship's dynamic impact load and crushing behaviour. To determine the dynamic structural response of the bridge piers subjected to ship collision, studies using FE methods (Gholipour et al., 2018) and simplified analytical methods were used (Fan et al., 2011) (Sha & Hao, 2014).

3. Methodology

3.1. Ship-bridge collision characteristics

3.1.1. Ship collision risk

Ship-bridge collisions can cause fatalities, economic losses, and environmental damage. Because of this, the risk of ship-collision must be managed carefully, such that the estimated frequency and consequence of such accidents remain low.

In the Oxford Advanced Learner's Dictionary, Risk is defined as “the possibility of something bad happening at some time in the future; a situation that could be dangerous or have a bad result” (Oxford, n.d.). The understanding and definition of risk will often vary depending on the industry, different stakeholders, and the implications of risk reduction measures (Chen et al., 2019). In engineering, the risk is often considered a product of the probability and potential consequence of an undesired event and can be expressed by equation 1.

$$R = P \times C \tag{1}$$

where

- R: The risk associated with the undesired event
- P: The probability of occurrence of an undesired event
- C: The expected consequence of the undesired event

(Kristiansen, 2005)

Because of the possibly severe consequences of ship collisions, it is crucial to manage the risks of ship collisions. One way to manage the risk is by performing frequent risk analyses, which typically are based on an estimation of the probability of the accident followed by an estimate of the consequences (Zhang et al., 2019c, p. 1).

3.1.2. Bridge acceptance criteria and design vessel selection

According to Zhang et al. (2019c), it is necessary to establish risk acceptance criteria for bridges to reduce and manage the risk of ship-bridge collisions.

Without it, it is impossible to find the balance between safety for the users and cost for the stakeholders. The risk acceptance criteria must be established for the following main risks:

- Fatalities
- Environmental damage
- Economic losses

According to Zhang et al. (2019c, p. 2), the acceptance criteria for fatalities related to shipping accidents are generally based on two principles:

- "The individual fatality risk shall be approximately the same as typical for other occupational hazards.
- The frequency of accidents with several fatalities, that is, the societal fatality risk, shall not exceed a level defined as unconditionally intolerable. Moreover, the general as low as reasonably practicable (ALARP) risk management shall be applied."

One way of managing the risks is by using F-N diagrams. Figure 3.1 shows an F-N diagram related to the number and frequency of fatalities.

- If the risk is in the 'negligible' region, the operation can continue without any risk reduction actions or assessments.
- If the risk is the 'intolerable' region, the bridge should shut down for operation.
- If the risk is in the 'ALARP' region, actions for risk reduction must be identified and evaluated, and the societal impact of such actions should be assessed. When the risk is in the 'ALARP' region, the additional cost of risk-reducing actions is evaluated against the consequence of the risk, and a condition for a decision to take risk-reducing actions was proposed by Zhang et al. (2019c, pp. 3-4). This condition is shown in equation 2 below.

$$Total\ costs < X + I + E + D \quad (2)$$

where

- X: Direct costs related to the accident
- I: Quantified change in the cost of all 'individual' user risks
- E: Quantified change of cost of environmental damage
- D: Economic costs caused by disruption

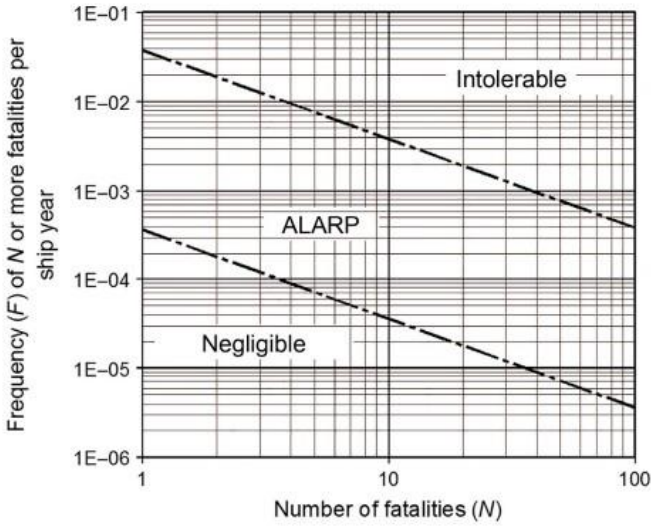

Figure 3.1 ALARP diagram (Zhang et al., 2019c)

For the design of bridges to resist and reduce the risks of ship collision, AASHTO (2009) proposes multiple risk acceptance criteria called 'Design Vessel Acceptance Criteria'. Such an acceptance criteria is global and distributed over the number of elements located within the waterway if the waterway is narrow, or within three times the ship length on each side of the vessel transit path if the waterway is wide. With given impact strength of the bridge structural elements, an impact probability analysis showing the frequencies of collision for the different bridge structural elements, and estimates of collision impact load for typical ship classes, it is possible to determine a design vessel for each bridge element (Zhang et al., 2019c, p. 49).

By definition, the design vessel is the ship size the structural elements of the bridge must withstand in the event of a collision to fulfil the acceptance criteria. In other words, for the bridge to fulfil the acceptance criteria, all impacts from ships of equal or smaller size than the design vessel should not lead to critical failure in the bridge element (Zhang et al., 2019c, p. 49).

AASHTO (2009, pp. 61-62) proposes three different methods for selecting the design vessel, each with different use cases and acceptance criteria:

- Method one: A simple, semi-deterministic procedure
- Method two: A more complicated, probability-based procedure
- Method three: A cost-effectiveness procedure

Method two is the most commonly used procedure, and the method deploys a probability-based analysis procedure to select the design vessel. The method is more complicated than the other methods, and it requires a significant amount of data for the vessel, bridge, and waterway characteristics. As this method is the most accurate, it should be used in most situations requiring an accurate risk assessment (AASHTO, 2009). When using method two to select the design vessel, the design vessel is selected based on the bridge operational classification, as well as the vessel, bridge, and waterway characteristics. Method two has the following acceptance criteria regarding the annual frequency of collapse for the bridge as a whole:

- Critical/essential bridges: The acceptable annual frequency of collapse should be equal to or less than 0.0001
- Typical bridges: The acceptable annual frequency of collapse should be equal to or less than 0.001

(AASHTO, 2009, p. 67)

3.1.3. The Heinrich Factor

The Heinrich factor originally described the relationship between accidents and injuries in the industrial sector and was introduced by H. W. Heinrich in 'Industrial Accident Prevention: A Scientific Approach' in 1959 (Heinrich, 1959).

For ship collisions, the Heinrich Factor describes the relationship between impacts that cause critical failure and all incidents that can initiate critical failure of the bridge (Pedersen et al., 2020). From an assessment and estimation of the frequency of ship collisions with ships of different types and sizes, one or multiple design ships are assigned to the bridge elements as described in chapter 3.2, and all collisions with ships of size less than the design ship for a specific bridge element should not cause critical failure in the bridge element (Jensen, 2017).

The probability of collapse of a bridge element subjected to a ship collision with a ship of size greater than the design vessel can be modelled as the Heinrich Factor. The Heinrich Factor depends on the ship type, ship size, bridge structure's impact velocity, strength, and other parameters (Pedersen et al., 2020).

According to Pedersen et al. (2020), there is a certain probability that no critical failure occurs in the event of a ship collision with a ship of size greater than the design vessel for the particular bridge element, and this may be due to two effects:

1. The kinetic energy (KE) of a colliding ship is reduced right before the moment of impact, typically due to late avoidance manoeuvres by the ship captain right before impact.
2. The bridge structural elements have additional capacity above the estimated capacity of the bridge structural elements.

The first effect deals with the reduction of the ship's KE right before the impact. As the impact speed is often reduced right before the impact due to last-second manoeuvres by the ship captain, the collision speed will be significantly reduced in many scenarios (Pedersen et al., 2020). Lutzen (2001) proved this by performing a survey of ship-ship collisions and observed that the speed of the striking vessel at the moment of impact is reduced and can be assumed to be generally distributed between a very low speed and the service speed. A reduced impact speed will naturally have a significant impact on the impact energy. Figure 3.2a shows this relationship. Similarly, the impact angle can significantly affect the impact energy. For collisions that are not head-on, sliding between the striking vessel and the bridge structural element can occur, resulting in less deformation and impact energy, as not all of the KE of the striking vessel is converted to internal strain energy in the bridge pier. Figure 3.2b shows this relationship. Here, the impact angle and friction coefficient will affect the impact energy (Pedersen et al., 2020). Note that in figure 3.2b, a 90º impact angle is a head-on collision, while a head-on collision in this study is taken as an impact angle of 0%.

The second effect concerns the reserve strength capacity of the bridge structural elements. The bridge design is typically based on characteristic loads and will therefore have an additional reserve capacity that will come into effect before critical failure occurs (Pedersen et al., 2020). Figure 3.2c shows this effect, where $Skib_{kar}$ indicates a ship equivalent to the bridge element's characteristic capacity, and $Skib_{max}$ indicates a ship equivalent to the bridge element's actual capacity.

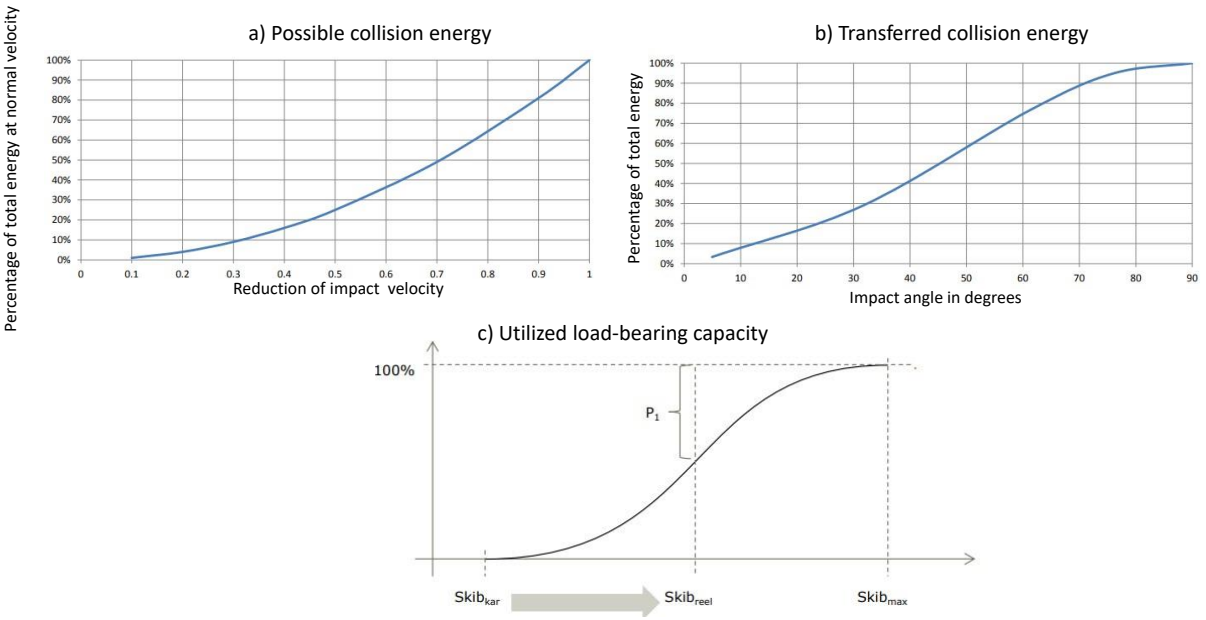

Figure 3.2 a) Possible collision energy as a function of the velocity reduction b) Transferred collision energy as a function of impact angle and c) Utilized load-bearing capacity

Due to these modifying effects, the probability of critical failure of a bridge element in the event of a ship collision can be expressed as:

$$P_{Critical\ failure} = P_{Critical\ failure\ |\ Collision} * P_{collision} \quad (3)$$

where

- $P_{Critical\ failure}$: The probability of a collision with a ship of greater size than the design vessel
- $P_{Critical\ failure\ |\ Collision}$: The Heinrich Factor which describes the probability of critical failure in the bridge element in the event of a ship collision with a ship of greater size than the design vessel
- $P_{collision}$: The probability of collision with a ship of size greater than the design ship

(Pedersen et al., 2020)

An exact calculation of the Heinrich Factor is impossible due to the uncertainties and varying conditions, and it must be estimated (Pedersen et al., 2020). AASHTO (2009, p. 78) estimates the Heinrich Factor as a function of the ratio between the ultimate bridge element strength and the vessel impact force, as shown in figure 3.3.

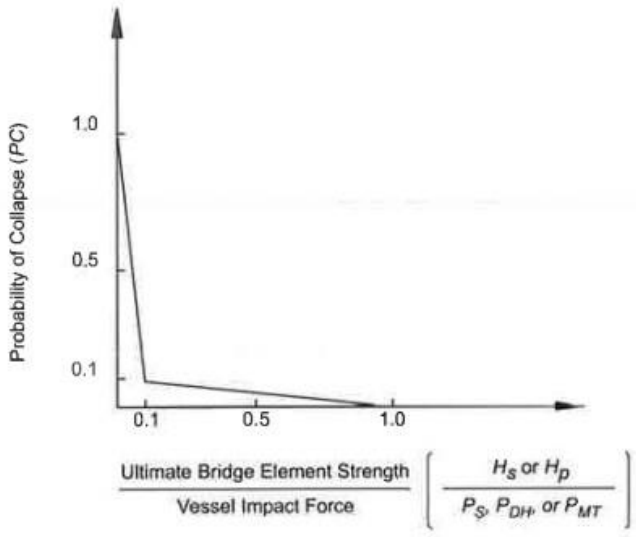

Figure 3.3 Distribution of the Probability of Collapse according to AASHTO (2009)

3.1.4. Impulse load and momentum

A collision involves the collision of two or more bodies. The forces each body involved in the collision exerts on another body are called impulse forces because of their large magnitude and short duration. However, as the collision forces are complex functions of time, it is impossible to directly determine the forces using Newton's Laws. Because of this, the terms 'momentum' and 'impulse' and the law of conservation of momentum is used to analyse collision forces (Alrasheed, 2019, p. 73).

Momentum is a measurement of how much mass is in motion and is proportional to the object's mass and velocity. Equation 4 shows the expression for momentum p.

$$p = m * v \tag{4}$$

According to Alrasheed (2019, p. 74), the impulse defines how a force acting on an object changes the linear momentum of the impacted object. If we consider a time-dependant force F acting on a particle, we can use the Newtons second law to express the impulse, shown in equations 5–11.

$$F = \frac{dp}{dt} \tag{5}$$

$$F = ma \tag{6}$$

$$dp = F\ dt \tag{7}$$

$$\int_{p_i}^{p_f} dp\ = \int_{t_i}^{t_f} F\ dt \tag{8}$$

$$p_f - p_i = \Delta p = \int_{t_i}^{t_f} F\ dt \tag{9}$$

The right side of equation 9 is known as the impulse, I, and equals the change in momentum $\int_{t_i}^{t_f} F\ dt$.

$$I = \int_{t_i}^{t_f} F\ dt \tag{10}$$

$$I = \Delta p \tag{11}$$

If the force F providing the impulse has a constant direction, the average force is expressed by equation 12. Furthermore, using equations 10 and 12, a new expression for the impulse is obtained (equation 13). The average force $\overline{F}$ is a constant force that gives the same impulse as the actual force F (Alrasheed, 2019, p. 74). An example of an impulse load determined by the force F and time Δt is shown in figure 3.4.

$$\overline{F} = \frac{1}{\Delta t}\int_{t_i}^{t_f} F\ dt \tag{12}$$

$$I = \overline{F}\,\Delta t \tag{13}$$

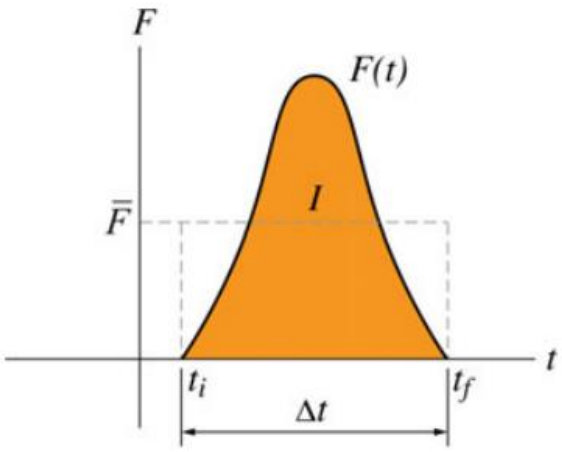

Figure 3.4 Example showing the variation of force F over time Δt (Alrasheed, 2019)

When considering a collision between two bodies, the system can be isolated during the short impact time, and the linear momentum is conserved during the collision. Any other forces present during the impact can be neglected because of the large magnitude and short duration of collision forces, and because of this, the force in equation 13 can be assumed to be the impulse load in isolation (Alrasheed, 2019, p. 75). This simplification of the collision response is called an impulse approximation. When applying the law of conservation of momentum in this case, equation 14 is obtained, where p_i is the momentum just before impact and p_f is the momentum just after impact. The law of the conservation of momentum is valid for ship-bridge collisions. However, as ship-bridge collisions are inelastic processes, some KE is lost to strain energy, primarily deformations (Alrasheed, 2019, p. 76).

$$p_i = p_f \tag{14}$$

3.1.5. Strain energy dissipation

The ship collision impact action is an accidental load characterised by the KE of the striking vessel, and equation 15 shows the KE expression. Some of the KE will remain as KE in the ship after the impact moment. Most of the energy that does not remain as KE dissipates as internal strain energy in the ship and structure, and will generally lead to large plastic strains and structural damage to the ship, structure, or both (NORSOK, 2013).

$$E_k = \frac{1}{2}mv^2 \quad (15)$$

According to NORSOSK N-004 (NORSOK, 2013), it is convenient to consider that the dissipation of strain energy in the structure occurs on three different levels:

- Local cross-section
- A component/sub-structure
- The total system

Plastic energy dissipation modes must be considered for the local cross-sections and components/sub-structures in direct contact with the striking vessel. Although the elastic strain energy can usually be disregarded, the elastic axial flexibility may significantly affect the load-deformation relationships for the components and sub-structures (NORSOK, 2013).

During a collision process between two bodies, the weakest body will dissipate most of the total strain energy. The process of strain energy dissipation will depend on the strength and ductility of the striking vessel and its structure. In NORSOK N-004 (2013), the design of a structure against ship collision is categorised into three design principles, depending on the relative strengths of the bodies. The design principles are discussed below, and the strain energy dissipation based on these design principles is shown in figure 3.5a.

- Strength design: When the structure is strong enough to resist the impact force with minor deformation, and where the ship will deform and dissipate a significant part of the collision energy.
- Ductility design: When the structure undergoes large, plastic deformations dissipate most of the collision energy, and the ship undergoes minor deformations.
- Shared-energy design: When both the ship and structure will deform significantly, both bodies contribute to the dissipation of the collision energy.

(NORSOK, 2013)

The structural responses of the ship and structure can be represented as load-deformation relationships and are illustrated in fig 3.5b. The total area under the load-deformation curves equals the strain energy dissipated by the ship and structure and can be expressed with equations 16 and 17.

$$E_{strain} = E_{strain,ship} + E_{strain,structure} \quad (16)$$

$$E_{strain} = \int_0^{w_{s,max}} R_s dw_s + \int_0^{w_{i,max}} R_i dw_i \quad (17)$$

where

R_s: Impact resistance of the ship

R_i: impact resistance of the structure

dw_s: deformation of the ship

dw_i: deformation of the structure

(NORSOK, 2013)

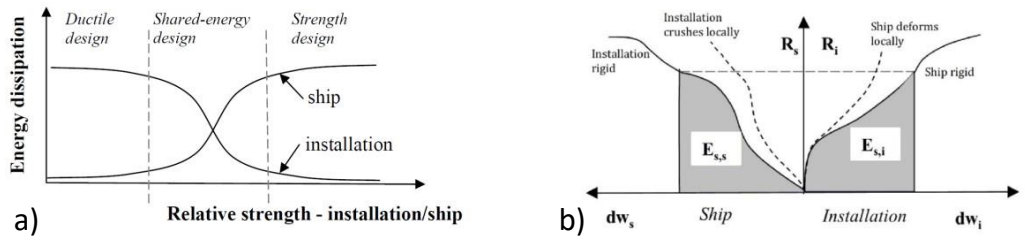

Figure 3.5 a) Energy dissipation for strength, ductile, and shared design and b) Dissipation of strain energy in ship and structure (NORSOK, 2013)

3.1.6. Collision mechanics

In the classical ship collision literature, the collision consequence estimation is typically separated into two independent problems:

- the external collision dynamics
- the internal collision dynamics

(Zhang et al., 2019a, p. 1)

The separation of the ship collision problem into two different problems is, in theory, only valid when the hydrodynamic pressure from the surrounding water on the ship hull can be modelled as constant added masses and the impact duration is very low such that the motion of the ships during the collision can be ignored (Zhang et al., 2019a, p. 1).

The external collision dynamics deals with the motion of the colliding bodies and their interaction with the water, and an external analysis is performed in two ways:

- Coupled analysis using time simulation procedures
- Uncoupled analysis using a mechanical approach

(Zhang et al., 2019a, p. 1)

Internal collision dynamics deals with the local crushing of material in the colliding bodies. The purpose of an external collision analysis is typically to establish force-penetration relationships and absorbed energy-penetration relationships for the collision. An internal collision analysis is performed in four ways:

- Empirical methods
- FE methods
- Experimental methods
- Simplified analytical methods

(Zhang et al., 2019b, p. 1)

3.1.7. Failure modes of reinforced concrete piers due to collision

In the event of a ship-bridge collision of a reinforced concrete pier subjected to a significant impact load, the bridge pier is subjected to large shear and bending forces which can lead to damage or collapse. In the event of a ship-bridge collision, multiple failure modes are possible. Buth et al. (2010) observed actual collision events between trucks and reinforced concrete piers, and figure 3.6 shows the typical failure modes.

According to Buth et al. (Buth et al., 2010), shear failure modes are most typical when the impact velocity is high. However, ship-bridge collision velocities are typically low. For lower impact velocity, the typical failure modes is a combined flexural-shear failure mode with flexural damages, which can lead to the formation of a plastic hinge during the impact response. Even though the formation of a plastic hinge may eventually lead to collapse, more time would have to be provided before the collapse, compared to the shear failure modes for which the time to collapse is relatively short (Gholipour et al., 2021).

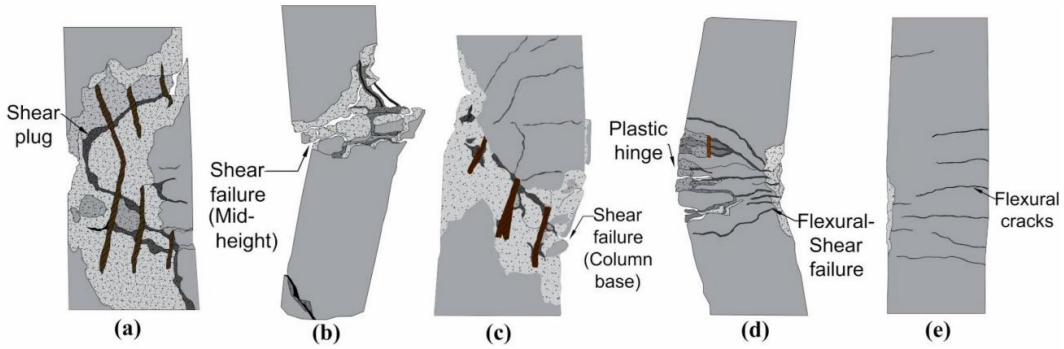

Figure 3.6 Typical failure modes of RC bridge piers subjected to collision loads; a) punching shear, b) shear hinge, c) diagonal shear failure, d) combined flexural-shear failure, e) flexural failure (Gholipour et al., 2021)

3.2. The FE Method

According to R. D. Cook (2002, p. 1), the FE method is a method for the numerical solution of field problems described by mathematical differential equations or integral expressions. Solving FE field problems requires the determination of the spatial distribution of one or more dependant variables. An interpolation function is used to interpolate the field variables of the element. Polynomials are the most used interpolation function. The degree of the polynomials will depend on the number of nodes connected to the element and will affect the simulation results and the computational cost of the simulation (Nikishkov, 2009).

In the FE method, the structure is divided into small, geometric elements called finite elements, which can be viewed as small pieces of a structure. The elements are connected with each other at the nodes, and the assembly of elements and nodes is called the FE mesh. The FE mesh can be numerically represented by algebraic equations to be solved for the unknowns at the nodal points (Cook et al., 2002, p. 1).

To obtain an efficient model with good accuracy and reasonable computation cost, it is crucial to discretise the structure into a reasonably detailed and efficient FE mesh. A more detailed mesh will include smaller elements and more nodes, which increases the accuracy and cost of the computation.

The FE system is generally defined by a mass matrix $[M]$, damping matrix $[C]$, stiffness matric [K], nodal displacement [D], and external loads $\{R^{ext}\}$. Equation 18 shows the general FE equation of motion. The Galerkin method of weighted residuals or the variational approach is the most commonly used method for solving the set of equations (Nikishkov, 2009). Along with the assumed field in an element, the solved unknown nodal values determine the spatial

variation of the field in the particular element, and the field quantity over the entire structure is approximated for each element. However, obtaining an exact solution to a FE problem is impossible, but it can be improved using smaller elements in the FE mesh (Cook et al., 2002, p. 1).

$$[M]\{\ddot{D}\} + [C]\{\dot{D}\} + [K]\{D\} = \{R^{ext}\} \quad (18)$$

According to Cook et al. (2002, pp. 1-2), the FE method has several advantages over other numerical analysis methods:

- FEA applies to any field problem: heat transfer, stress analysis, magnetic fields, etc.
- There is no geometric restriction, and the body analysed can have any shape.
- Boundary conditions, loading, and material properties are not restricted and may change from one element to another.
- The FE structure resembles the actual body to be analysed.

FEA is performed with the use of FE Software and the FEA in general consists of the following main steps:

- "Pre-processing: Input data like the geometry, loads and boundary conditions are defined, and the model is discretised to an FE mesh.
- Numerical analysis: The software solver generates the FE equations that define the system and solves the system equations.
- Postprocessing: The solutions from the numerical analysis are listed or graphically presented."

(Cook et al., 2002, p. 13)

3.2.1. LS-Dyna

LS-Dyna is a general FE software for analysing large deformations and dynamic, nonlinear responses of structures and is the software used for the FEA in this study. The software is widely used in the car industry (crash testing), aerospace, construction, and other industries (LSTC, n.d.-e). LS-Dyna is mainly a solution methodology based on explicit time integration, but an implicit time integration solution methodology is also available (LSTC, n.d.-e).

LS-Prepost is an advanced pre- and post-processor and part of the LS-Dyna product (LSTC, n.d.-f). LS-Prepost is the pre-processor tool used to create the FE model and to analyse the

simulation results. The FE modelling of complex structures can be an advanced and time-consuming process, and knowledge of the analysis method and tool is crucial to get correct results. If the user of the FE programme lacks knowledge about the analysis method/tool, the consequences can be devastating (Cook et al., 2002, p. 1).

FE modelling of structures in LS-Dyna consists of the following main steps:

- Modelling of the geometry and mesh
- Modelling of the materials and sections
- Modelling of the other relevant properties of the structure, like contact formulations, constraints, and boundaries

The simulations were performed using the Software LS-Run, which acts as a graphical control centre for running the numerical analysis in LS-DYNA. Various command-line options are used to activate different options for the analysis. The most common command-line options are the input file, memory usage, the number of processes for the analysis, and the LS-DYNA executable file (Jernberg et al., 2018).

3.2.2. Structural dynamics in FEA

A FE problem can be time-independent (static) or time-dependent (dynamic). In a static problem, no time variation exists, and the system can be solved by direct solution methods or iterative solution methods (Neto et al., 2015, p. 60).

However, if the loading is of a higher frequency or is applied suddenly, the problem can be assumed to be time-dependent (dynamic), and dynamic analysis must be used to determine the response (Cook et al., 2002, p. 373). The equation of motion for dynamic problems is shown in equation 18. Implicit and explicit direct integration methods, modal methods, and the related Ritz vector method are commonly used to determine the response history of a dynamic problem (Cook et al., 2002).

3.2.3. The explicit and implicit direct integration methods

The direct integration method to calculate the response history uses a step-by-step integration procedure, where the response is calculated at each time-step until the final, nth timestep is

reached ($t_0, t_1, t_2, \dots, t_n$). The time step increment Δt separates each time step (Cook et al., 2002, p. 407). The dynamic equation of motion at the nth time step is shown in equation 19.

$$[M]\{\ddot{D}\}_n + [C]\{\dot{D}\}_n + [K]\{D\}_n = \{R^{ext}\}_n \quad (19)$$

The conditions are calculated at time step t+1 with the equation of motion, a difference expression, and known conditions at one or multiple preceding times with direct integration methods. Direct integration methods are categorised into an implicit and an explicit integration algorithm.

The implicit procedure uses information about the velocity and acceleration at the current time step and historical information to determine the condition at the time step n+1. Equation 20 shows the implicit difference expression.

$$\{D\}_{n+1} = f(\{\dot{D}\}_{n+1}, \{\ddot{D}\}_{n+1}, \{D\}_n, \{\dot{D}\}_n, \{\ddot{D}\}_n, \dots) \quad (20)$$

The explicit procedure uses only historical data to calculate the conditions at time step n+1, and the explicit difference expression is shown in equation 21. The procedure is based on using an explicit integration rule, typically the central difference integration rule, which is discussed in chapter 3.2.4 (Cook et al., 2002, p. 47).

$$\{D\}_{n+1} = f(\{D\}_n, \{\dot{D}\}_n, \{\ddot{D}\}_n, \{D\}_{n-1}, \dots) \quad (21)$$

The most significant differences between the implicit and explicit methods are related to computational cost and stability. In explicit methods, the coefficient matrix of $\{D\}_{n+1}$ can be made diagonal. Because of this, $\{D\}_{n+1}$ can be easily calculated at each time step, compared to implicit methods, where $\{D\}_{n+1}$ cannot be made diagonal.

Regarding stability, the explicit methods are conditionally stable, which means that the critical time step Δt_{cr} cannot be exceeded if the numerical process is to remain stable. As the critical time step Δt_{cr} is typically relatively small, the explicit method requires many time steps compared with the implicit method, which remains stable for more considerable time steps.

To summarise, the explicit methods need more time steps but low cost per time step, while the implicit methods need fewer time steps but more computational cost for each time step. The explicit method is preferred for wave propagation problems, which arise from blast or impact

actions. In contrast, the implicit method is preferred when the load varies slowly, such as for earthquake loads (Cook et al., 2002, pp. 408-409).

The ship-bridge collision problem in this study is a wave propagation problem and involves a dynamic, explicit integration method to determine the structural response. Because of this, an in-depth description of the explicit integration method and the explicit central difference integration scheme follows in the next chapter.

3.2.4. Central difference method

The explicit direct integration method is performed using the central difference method. In the central difference method, the solution domain is replaced with a finite number of points, commonly called grid points, and the response is solved at the grid points. Two common variations of the central difference method are the classical central difference scheme and the half-step central difference scheme, and both are explained briefly below.

Classical integration method

The central difference approximations can be derived using the Taylor series expansion of $\{D\}_{n+1}$ and $\{D\}_{n-1}$ shown in equations 22 and 23 . To obtain the central difference velocity expression in equation 24, equation 23 is subtracted from equation 22 and to obtain the central difference acceleration expression in equation 25, equation 22 is added to equation 23. Note that the terms Δt of power higher than two are disregarded. By combining equations 19, 24 and 25, equation 26 is obtained, which is an alternative expression for the equation of motion.

$$\{D\}_{n+1} = \{D\}_n + \Delta t\{\dot{D}\}_n + \frac{\Delta t^2}{2}\{\ddot{D}\}_n + \frac{\Delta t^3}{6}\{\dddot{D}\}_n + \cdots \quad (22)$$

$$\{D\}_{n-1} = \{D\}_n - \Delta t\{\dot{D}\}_n + \frac{\Delta t^2}{2}\{\ddot{D}\}_n - \frac{\Delta t^3}{6}\{\dddot{D}\}_n + \cdots \quad (23)$$

$$\{\dot{D}\}_n = \frac{1}{2\Delta t}\left(\{D\}_{n+1} - \{D\}_{n-1}\right) \quad (24)$$

$$\{\ddot{D}\}_n = \frac{1}{\Delta t^2}\left(\{D\}_{n+1} - 2\{D\}_n + \{D\}_{n-1}\right) \quad (25)$$

$$\left[\frac{1}{t^2}M+\frac{1}{2\Delta t}C\right]\{D\}_{n+1}=\{R^{ext}\}_n-[K]\{D\}_n+\frac{2}{\Delta t^2}[M]\{D\}_n-\left[\frac{1}{\Delta t^2}M-\frac{1}{2\Delta t}C\right]\{D\}_{n-1} \quad (26)$$

(Cook et al., 2002, pp. 409-410)

Half-step integration method

With the half-step central difference method, the velocity and acceleration are approximated as shown in equations 27, 28 and 29. The equation of motion shown in equation 19 can then be altered by lagging the velocity by one half time-step, and is shown in equation 32. By combining equations 27, 28 and 29 , equation 30 is obtained.

$$\{\dot{D}\}_{n-\frac{1}{2}}=\frac{1}{\Delta t}(\{D\}_n-\{D\}_{n-1}) \quad (27)$$

$$\{\ddot{D}\}_n=\frac{t}{\Delta t}\left(\{\dot{D}\}_{n+\frac{1}{2}}-\{\dot{D}\}_{n-\frac{1}{2}}\right)=\frac{1}{\Delta t^2}(\{D\}_{n+1}-2\{D\}_n+\{D\}_{n-1}) \quad (28)$$

$$[M]\{\ddot{D}\}_n+[C]\{\dot{D}\}_{n-\frac{1}{2}}+[K]\{D\}_n=\{R^{ext}\}_n \quad (29)$$

$$\frac{1}{\Delta t^2}[M]\{\ddot{D}\}_n=\{R^{ext}\}_n-[K]\{D\}_n+\frac{1}{\Delta t^2}[M]\left(\{D\}_n+\Delta t\{\dot{D}\}_{n-\frac{1}{2}}\right)-[C]\{\dot{D}\}_{n-\frac{1}{2}} \quad (30)$$

(Cook et al., 2002, p. 410)

Stability of the explicit direct integration scheme

In the classical central difference scheme, the integration is conditionally stable as long as $\Delta t \leq \frac{2}{\omega_{max}}=\Delta t_{cr}$ or $\Delta t \leq \frac{T_{min}}{\pi}$. The stability of the half-step integration scheme depends on the damping coefficient, as it is stable as long as $\Delta t \leq \frac{2}{\omega_{max}}(\sqrt{1-\xi^2}-\xi$, where ξ is the damping ratio in the ω_{max} mode. The frequency ω_{max} is the highest natural frequency of the system $([K]+\omega^2[M])\{D\}=\{0\}$ (Cook et al., 2002, p. 411).

If the time step Δt is too large, the explicit integration becomes unstable and fails, while too small of a time step may lead to unnecessary high computational cost. It is therefore important to estimate the critical time step, Δt_{cr}, such that $\Delta t<\Delta t_{cr}$. From the stability expressions above, Δt_{cr} depends on ω_{max} of the system. Therefore, to estimate Δt_{cr}, ω_{max} of the system must be determined. One way to do this without having to assemble [K] and solve the eigenvalue

problem is to note that it must be smaller than ω_{max} of any unassembled and unsupported element in the FE system. By following the procedure, the CFL (Courant-Friedrichs-Lewy) condition $\Delta t_{cr} \leq \frac{L}{c}$ is obtained, where L is the length of the material and c is the speed of sound in the material (Cook et al., 2002, pp. 412-413).

3.2.5. Nonlinear FEA

Up until now, we have only focused on linear FEA, and for this type of problem, the equation of motion in equation 18 is applicable. However, FE problems can be nonlinear. With the rapid development in computer power and FEA in general, nonlinear FEA can be performed and nonlinear FE problems can be solved (ABS, 2021). For nonlinear FE problems, the term $[K]\{D\}$ is replaced with $\{R^{int}\}$ (internal loads) to accommodate material nonlinearity. Equation 31 shows the equation of motion for nonlinear FEA.

$$[M]\{\ddot{D}\}_n + [C]\{\dot{D}\}_n + \{R^{int}\}_n = \{R^{ext}\}_n \quad (31)$$

Materials may yield or creep in structural engineering applications, and local damage or buckling can occur. The primary sources of nonlinearities in engineering applications are material nonlinearity, geometric nonlinearity, and boundary condition nonlinearity. Material nonlinearity typically occurs for large strains, and nonlinear stress-strain curves can characterise the nonlinear behaviour. Geometric nonlinearity occurs in beams and shells for large displacements, such that the applied load or stiffness depends on the structure's geometry. In contrast, boundary condition nonlinearity might occur when two or more bodies contact one another and interact (Cook et al., 2002, pp. 595-626).

In these types of problems, the stiffness matrix [K] and possibly the load vector [R] are functions of displacement [D]. As the information needed to construct the stiffness matrix [k] and load vector [R] is unknown, an iterative process must obtain the displacement and the associated stiffness and loads such that equation 31 is in equilibrium.

The explicit and implicit direct integration methods discussed in chapter 3.2.3 are valid for nonlinear FE problems as well. Because the explicit method accommodates smaller time steps and uses less computational time per time step than the implicit method, the explicit method is preferred for nonlinear problems (Cook et al., 2002, p. 616).

3.2.6. Damping

Damping is the dissipation of energy due to decaying free vibration amplitude with time and the limiting of the free vibration amplitude from a loading whose frequency coincides with the natural frequency of the vibrating body. Damping is usually added to a FE system to avoid resonance and limit the peak response of vibrations (Cook et al., 2002, p. 388).

The three main types of damping that affect the structural dynamics are viscous damping, hysteresis damping, and coulomb damping. Viscous damping is the most common type of damping. In the case of viscous damping, a force proportional to the velocity is applied, and the term $[C]\{\dot{D}\}$ expresses the viscous damping in the equation of motion (equation 18). Viscous damping is applied to a FE system by surrounding gas, surrounding liquid, or with viscous dampers. Viscous damping is often referred to as proportional damping or Rayleigh damping

If viscous damping is present in a FE system, there exists a critical damping value $C_c = 2m\omega$. If the damping coefficient $C > C_c$ the vibrating motion decays without oscillations, while if $C < C_c$ the motion oscillates and decays with time. In the case of $C < C_c$, the damped vibration frequency ω_d is less than the natural frequency. Equation 32 shows the relationship between ω_d, ω and ξ.

$$\omega_d = \omega\sqrt{1 - \xi^2} \tag{32}$$

where

$$\xi = \frac{c}{c_c} \; and \; c_c = 2m\omega \tag{33}$$

ξ denotes the ratio of damping to critical damping and is called the damping ratio (Rao, 2018, pp. 189-194). In structural problems, the damping is typically relatively small, and can be modelled sufficiently by regarding the damping as viscous (Cook et al., 2002, p. 389).

3.2.7. Plasticity

Plasticity refers to the part of the mechanism that deals with calculating stresses and strains in a ductile body permanently deformed by external forces (Chakrabarty, 2006, p. 1). Most materials display a linear elastic response to a load before yielding for engineering applications, and the stresses and strains can easily be calculated using the elastic constants and strains.

However, the load, deformation, and stress become nonlinearly related and history-dependent when the material yields. As the final state of stress and strain are history-dependent, the history must be considered by formulations that relate increments of stress to strain to determine the final state of deformation when plasticity is considered (Cook et al., 2002, p. 606).

According to Fjær et al. (2021, pp. 126-127), the theory of plasticity is based on four major principles:

1. Plastic strain. The total increment of the strain associated with the total increment of stress is assumed to include an elastic part and a plastic part, as shown in equation 34. $d\varepsilon_{ij}^{e}$ is related to the elastic stress increment and will vanish after the stress is removed and $d\varepsilon_{ij}^{p}$ is related to the plastic stress increment and will remain after the stress is removed.

$$d\varepsilon_{ij} = d\varepsilon_{ij}^{e} + d\varepsilon_{ij}^{p} \quad (34)$$

2. A yield criterion. The yield point is the point of a stress-strain curve where irreversible plastic deformations begin to occur, and the yield criterion defines the range of stresses where plasticity occurs.
3. A flow rule, which describes how the plastic strains develop in the material for given loading conditions.
4. A hardening rule. The ability of a material to sustain an increasing load after initial failure under certain conditions.

The hardening is typically decomposed into two modes; isotropic hardening and kinematic hardening. Isotropic hardening implies that the yielding surface expands or shrinks uniformly about the hydrostatic axis, while kinematic hardening is a translation of the failure surface in the stress space. To realistically represent the hardening of materials, the hardening is best described as a combination both modes (Fjær et al., 2021, p. 134). Figure 3.7 shows the difference between isotropic and kinematic hardening.

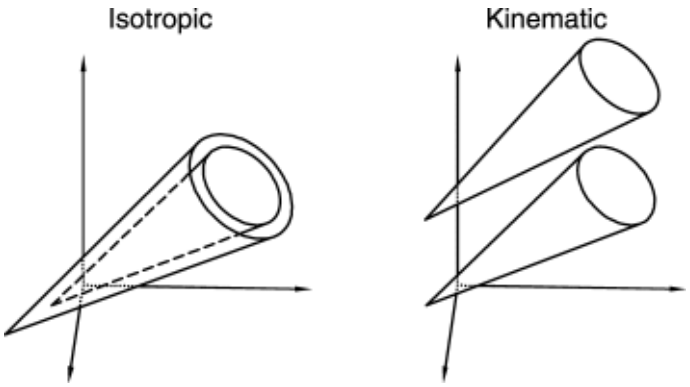

Figure 3.7 Isotropic and kinematic hardening (Fjær et al., 2021)

3.2.8. Elements in FEA

The discretisation of a structure into small, finite elements is an integral part of FEA and is one of the first steps when creating a FE model. The assembly of the elements defines the model's geometry, and the elements are assigned material properties, section properties, and other properties. Each finite element is connected to a set of nodes. When multiple elements are assembled, the DOF of each finite element are merged into a single set of global DOF at the shared nodes (Cook et al., 2002). The typical elements used in FEA include beam, solid, shell, and discrete elements.

Beam elements

A beam element is a finite element defined between two nodes. A 3D beam element has six DOF at each end node (three translatory and three rotational). Additionally, a third node can be introduced to determine the orientation of the cross-section and is required for specific beam formulations (LSTC, 2021a). The Euler Bernoulli and Timoshenko beam theories are the most commonly used beam elements. The Euler Bernoulli beam theory assumes that the transverse shear deformation can be ignored when considering bending deformations. In contrast, the Timoshenko beam theory considers the transverse shear deformation when considering bending deformation (Cook et al., 2002, p. 24).

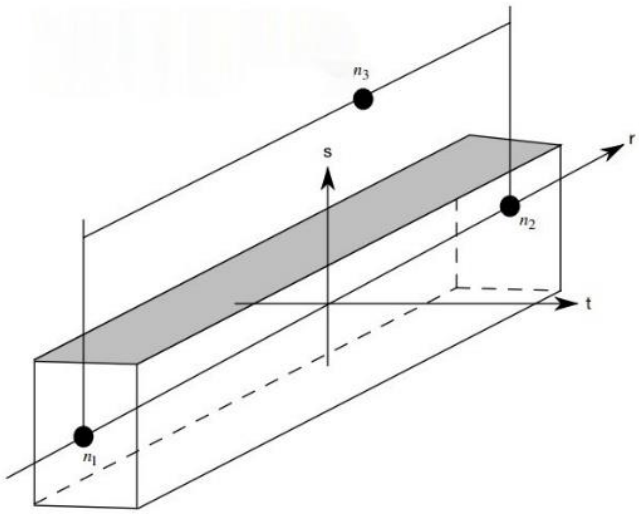

Figure 3.8 Beam element with 3 nodes in LS-DYNA (LSTC, 2021a)

Another beam element type is the discrete element. It is also defined between two nodes, but has only one DOF. It is used to model simple springs or dampers in a spring-mass system. The spring/damper can be translational or rotational, and it can be assigned force-displacement curves and other properties with the *MATERIAL keyword (LSTC, 2021a).

Solid elements

Solid bodies and structures were modelled with 3D solid elements. It can have any arbitrary shape, material property, and boundary conditions in space. The solid element has six possible stress components, three normal components, and three shear components (Liu & Quek, 2013). The most common solid element is the solid rectangular element, also called hexahedrons. These elements typically have 8 or 20 nodes, with 24 and 60 DOF, respectively (Cook et al., 2002, pp. 102-103).

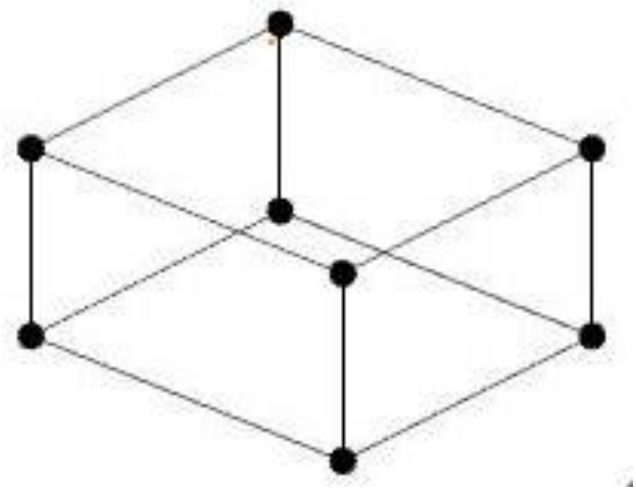

Figure 3.9 Solid 8-noded element (LSTC, n.d.-b)

Shell elements

Shells are elements of flat or curved outer and inner surfaces, and the thickness of the shell separates the surfaces. Shell elements are typically triangular with three or six nodes or rectangular with four or eight nodes with six DOF (three translatory and three rotational) at each node (Cook et al., 2002, pp. 91-98). The stress in a shell element generates membrane forces. Bending and twisting moments are also present in a shell element, and the stress state of a shell can be represented as the superposition of the membrane forces and bending stresses (Cook et al., 2002, p. 561).

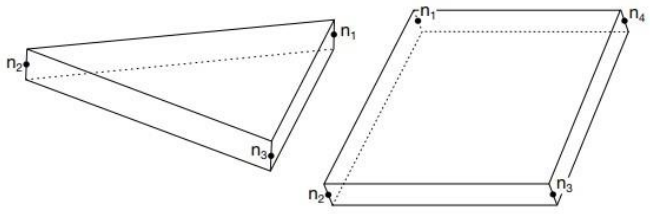

Figure 3.10 Triangular and quadrilateral shell elements (LSTC, 2021a)

3.2.9. Hourglass modes

Hourglass modes are non-physical, zero-energy modes of deformation that produce zero strains and occur in under-integrated solid and shell elements (LSTC, n.d.-c). The hourglass modes must be controlled when using one-point integration solid or shell elements. However, the

hourglass modes are likely to have shorter periods than the structural response period and this is the most significant disadvantage of using one-point integration elements (LSTC, 2021a).

In LS-Dyna, the LS-Dyna keyword *HOURGLASS applies the hourglass control. The commonly used hourglass formulation types are the viscosity-based hourglass control (hourglass formulation 1–3) and the stiffness-based hourglass control (hourglass formulation 4–5). The viscosity-based hourglass control generates hourglass forces proportional to the nodal velocity components contributing to the hourglass modes and is the preferred hourglass formulation for high velocity/strain problems and problems involving explosives. (LSTC, n.d.-d). However, the stiffness-based formulation generates hourglass forces proportional to the nodal displacement components contributing to the hourglass modes and is preferred for lower-rate problems, including crash and impact analyses (LSTC, n.d.-d).

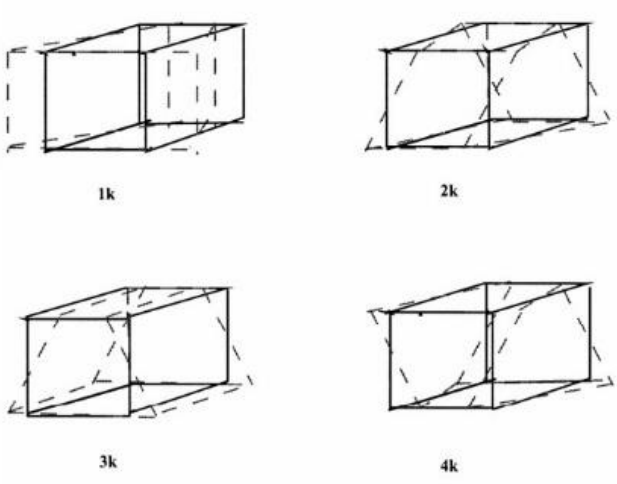

Figure 3.11 Hourglass modes of an eight-node element with one integration point (LSTC, 2006)

3.2.10. Material modelling in FEA

Concrete

Concrete is one of the essential materials for civil and structural engineering. Concrete is characterised by high compressive strength, but it must be combined with steel rebars to manage high tensile stresses. In combination, concrete and steel form a highly effective structural material that can manage heavy loads in both tension and compression. Additionally, reinforced concrete is economical, versatile, and durable if designed correctly (Hanses, 2015). Because of

these properties, reinforced concrete is one of the most used building materials for bridge construction.

Figure 3.12 shows a typical stress-strain curve for concrete. Initially, the stress-strain relationship is linear, and the concrete behaves elastically. The elastic part of the stress-strain relationship is characterised by uniform deformation. In the second part, the material modulus starts to decrease, and the stress-strain relationship is nonlinear due to the damage induced by the high stresses. After the stresses reach the peak compressive strength, the stresses required to induce further strains rapidly decrease due to fractures/big cracks in the material (Li, 2011).

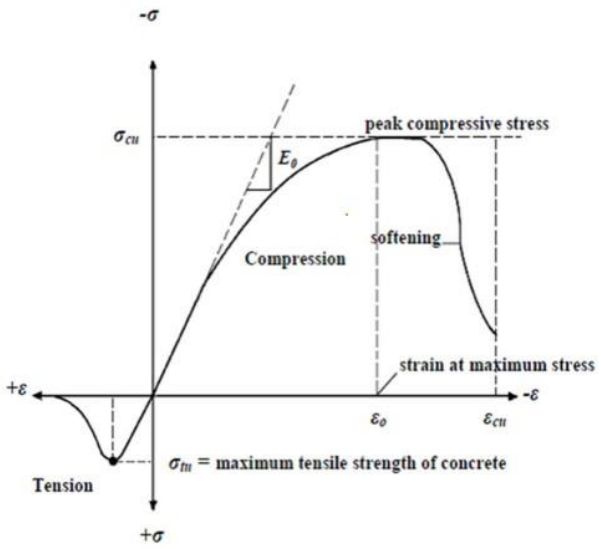

Figure 3.12 Typical stress-strain curve for concrete (Kh et al., 2016)

Steel

Like concrete, steel is one of the most used building materials for civil and structural engineering. The main advantages of steel are the ductility, low weight, and high strength in both compression and tension. Steel can be used as the primary material of bridges, particularly for long-span bridges or bridges in areas with seismic activity (Lin & Yoda, 2017, p. 61). Steel is also widely used along with concrete as reinforcement rebars in the longitudinal and transverse directions.

Figure 3.13 shows a typical stress-strain curve for hot-rolled carbon steel. Initially, the stress-strain relationship is linear, and the material deforms elastically. The stress-strain slope can be described with the young's modulus in this range. After the stress reaches the yield stress, f_y,

the strain will continue to increase without any increase in stress until the strain reaches the strain hardening strain ε_u, and the strain hardening phase begins. During the strain hardening phase, the stress increases with increasing strain until the stresses reach the maximum ultimate tensile strength. For stresses above the ultimate tensile strength, f_u, necking and eventually fracture occurs, and the stress required to increase the strain decreases (Gardner et al., 2019).

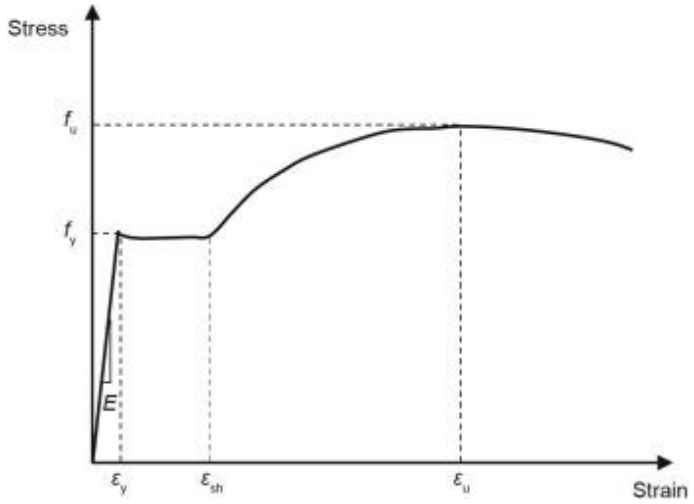

Figure 3.13 Typical stress-strain curve for carbon steel (Gardner et al., 2019)

3.2.11. Contact in FEA

Contact is an essential aspect of mechanical systems and FE collision analyses. In the case of a collision between two or more bodies, contact occurs between the surfaces of the bodies so that they cannot overlap in space. Contact is categorised as boundary nonlinearity and consists of two aspects. First, in the case of contact between two separate bodies, the contact force will remain zero until the impact. After the impact, the contact force increases vertically, and it is impossible to establish a functional relationship between the contact force and the displacement. Secondly, in the case of a typical problem in mechanics, the contact force or the displacement is given at specific material points, and the FE equation solves for the unknown contact force or displacement (Kim, 2015, pp. 567-568).

However, in contact, both the displacement and contact force are unknown, and it has to be determined whether the material point in the boundary of the body is in contact with another body. If so, the contact force is to be calculated. As the contact forces at different material points

might affect the displacement of adjacent material points, this process must be repeated until finding the correct states for all possible points in contact (Kim, 2015, p. 468).

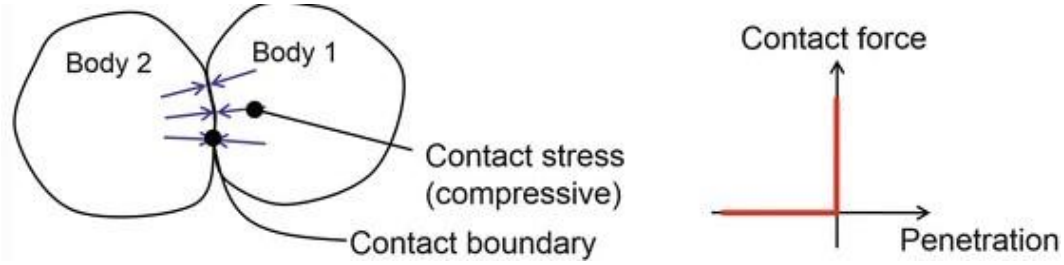

Figure 3.14 Contact boundary and contact force (Kim, 2015)

The slave-master contact concept is a commonly used contact concept used in FEA. For this concept, one body is identified as a slave, and the other is identified as a master. The contact formulation is imposed such that the surface nodes of the slave body cannot penetrate the surface nodes of the master body (Kim, 2015, pp. 568-569).

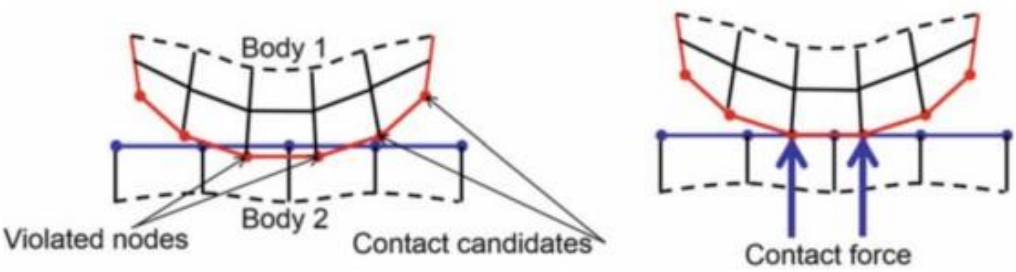

Figure 3.15 Contact search and force (Kim, 2015)

Accurate modelling of the contact formulation is crucial for the prediction capabilities of the FEA in the case of a collision analysis. In LS-Dyna, contact is defined by identifying what locations must be checked for penetration. LS-Dyna uses the slave-master contact concept discussed above to define the penetration, and at each time step, a search for penetration is done. The most commonly used approach for calculating contact forces is penalty-based contact. It uses a finite stiffness approach, with elastic compression-only springs in the normal direction to resist and eliminate penetration by applying a force proportional to the penetration depth. Some significant advantages of penalty-based contact are that it tends to be stable and does not cause mesh hourglassing (LSTC, n.d.-a).

According to LS-DYNA (LSTC, n.d.-a), the predetermination of where and how contact will occur can be difficult. For this reason, the automatic contact options are recommended as these contacts are non-oriented, meaning they can detect penetration coming from either side of a shell element" (LSTC, n.d.-a). Because of this, automatic contact types are used in the FE model. The specific contact formulations used in the FE model are discussed in chapter 4.5.

The deformation in impact analyses can be extensive, and it can be challenging to predetermine where and how the contact will occur. This problem can be solved using LS-Dyna's automatic contact search algorithms, which can be identified with the *AUTOMATIC in the *CONTACT keyword. With the automatic contact algorithm, contacts that are non-oriented can be identified, which makes the automatic contact algorithm more suited for handling disjointed meshes, which often occur in impact analyses (LSTC, n.d.-a).

LS-Dyna's major contact formulation types include the one-way treatment of contact, two-way treatment of contact, tied contact, and single surface contact. The one-way contact treatment allows the transfer of compression loads between the slave nodes and the master segments, and only the user-specified slave nodes are checked for penetration of the master segment (LSTC, n.d.-a).

The two-way contact treatment works essentially the same way as the one-way treatment, but after the slave nodes are checked for penetration of the master segment, the master nodes are checked for penetration of the slave segments. This type of contact treatment is symmetric. The definition of the slave and master segments is arbitrary for the two-way treatment, at the cost of increased computational cost due to the extra subroutine (LSTC, n.d.-a).

The slave nodes are constrained to move the master surface in the tied contact treatment. At the start of the simulation, the closest master segment to each slave node is located. If the slave node is close to the master segment based on established criteria, the slave node is moved to the master surface. The self-contact of the same or different elements is defined with the single surface contact treatment. It is a reliable and accurate contact type for defining self-contact (LSTC, n.d.-a).

3.3. Machine learning theory

According to Zhou (2021, p. 2), "Machine learning is the technique that improves system performance by learning from experience via computational methods". It uses experience in the

form of data and develops learning algorithms that use the data to build models. The model can eventually make predictions on new observations based on the training data using learning algorithms.

The first step when conducting machine learning is to gather data, which collectively form the dataset. The dataset contains records, and each record contains information about an event of an object. It describes some attributes about the event/object, and these descriptions are often called attributes, and their values are called attribute values. An example could be a dataset containing personal information, where height and nationality are the attributes, and '185 cm' and 'Norwegian' are the attribute values.

The data that learning algorithms use to build models are called training data, and the process of using machine learning to build models is called learning. In addition to experience, it is necessary to have some information about the outcome to train a prediction model effectively, called training data. The main vectors of a neural network are weights and bias variables. What occurs in the machine learning process is that it checks for similarities between the input and the training data. If the input is similar to some training data, it will yield the same output for this particular training data. If not, the machine learning process adjusts the weights and bias variables to make a better prediction at the next iteration.

The problem is a multiclass classification problem if the prediction output is discrete, and more than two classes are present. Suppose the prediction output is discrete with only two outputs, 'yes' or 'no.' In that case, the problem is a binary classification problem, where one class is positive ('yes') and one class is negative ('no'). If the prediction output is continuous, it is typically called a regression problem (Zhou, 2021).

Generally, with machine learning, the objective is to establish a mapping $f: x \rightarrow y$ from the input space x to the output space y by learning from a training set $\{(x_1, y_1), (x_2, y_2), \dots, (x_n, y_n)\}$. The output will depend on the type of prediction output. For binary classification problems, the output space is conventionally set as positive or negative, or $y = \{0, 1\}$ (Zhou, 2021).

4. FE Setup in LS-Dyna

4.1. The FE model

The FE model is a simplified model of a non-existent bridge. The bridge has four spans, and each span has length 30 m. Figure 4.1 shows the bridge model. The FE bridge model is divided into three smaller sub-models, which are:

- The local, detailed FE model of the pair of bridge piers in the middle of the bridge's longitudinal direction, including its pier and pile cap, and pile foundation supporting the piers. Figure 4.2 shows the local model.
- The global FE bridge model includes a simplified model of the bridge deck, bearing/abutments, and the piers at the left and right to the bridge piers of the local model. Figure 4.8 shows the global bridge model.
- The FE ship model. Figure 4.9 shows the ship model.

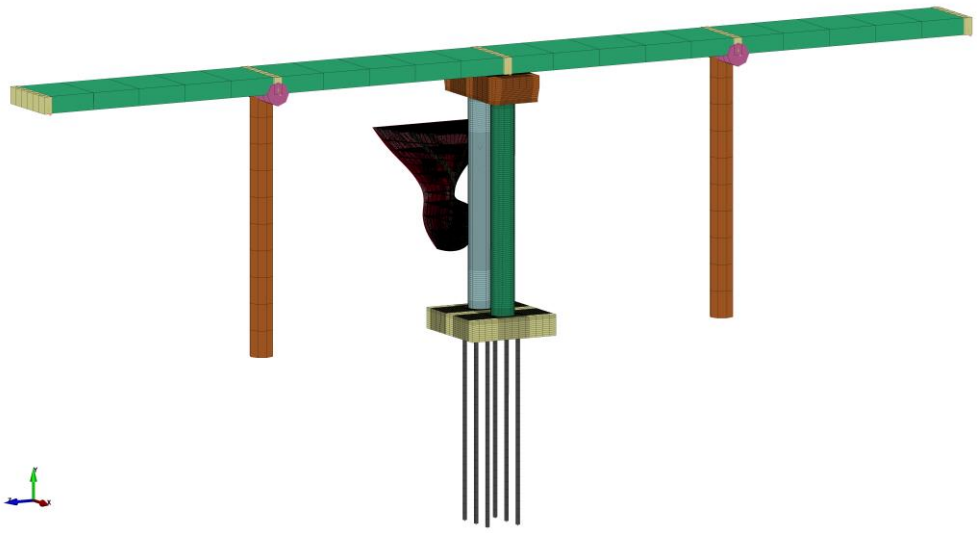

Figure 4.1 Bridge model in LS-Dyna

4.2. The local model

The local FE model of the bridge piers is modelled with a detailed mesh, and consists of three parts. The three parts are as follows:

- The bridge piers (including reinforcements)
- The pier and the pile cap
- The foundation piles and the soil-pile interaction

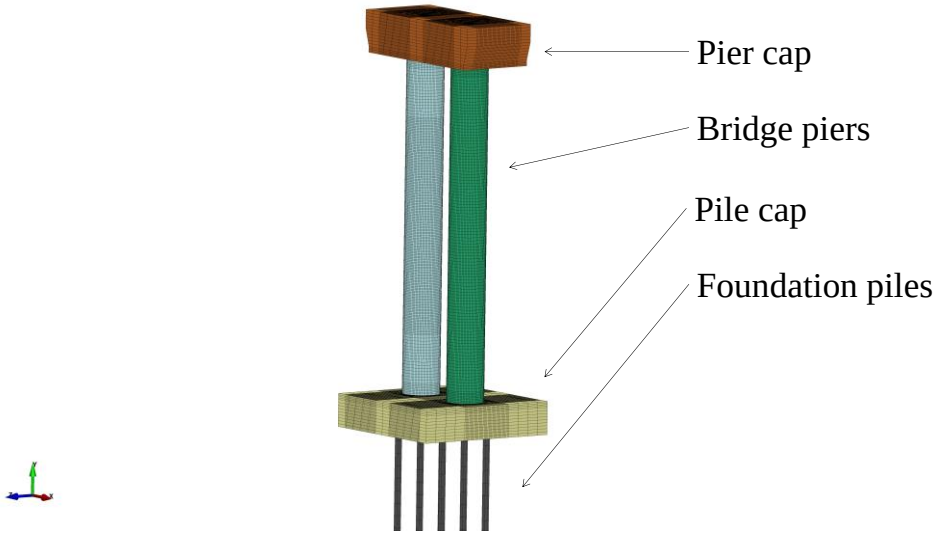

Figure 4.2 The local bridge model

4.2.1. Bridge piers

The circular bridge piers are 25.2 m high, have diameter 2.8 m and are located 2.9 m apart from each other. The bridge pier material is reinforced concrete (B45 concrete and B500 steel). The piers are connected to the pier and the pile cap by merging the shared nodes.

The impacted bridge pier has a detailed mesh at the middle section, where the impact is located, and at the top and bottom sections, where it is connected to the pier and the pile cap. For the other sections, the mesh was less detailed. The second bridge pier, which will not be stuck by the ship, is meshed with a less detailed mesh compared to the impacted pier.

The piers are modelled using under-integrated constant stress solid elements, and each element consists of eight nodes and 24 DOF. As mentioned in chapter 3.2.8, it is an efficient and accurate element formulation, but it needs hourglass stabilisation. Because of this, the elements are assigned a stiffness-based hourglass control (hourglass formulation four with hourglass coefficient 0.05. The hourglass coefficient is low to minimize the non-physical stiffening of the response but still effectively inhibits the hourglass modes (LSTC, n.d.-c).

The material model *MAT_CONCRETE_DAMAGE_REL3 was used to model the concrete. The material model uses a three-invariant model and three shear failure surfaces and includes the effects of damage and strain rate (LSTC, 2021a). *MAT_ADD_EROSION keyword is added to the pier material model to consider material failure (LSTC, 2021a). The material properties of the piers are shown in Table 4.1. In addition to the properties below, the material model required the input of the strain rate effects. The strain rate effects are a curve, with the effective strain on the abscissa (negative=tension) and strength enhancement on the ordinate (LSTC, 2021b). The values for the strain rate effect for the concrete are taken from the LS-Dyna keyword manual for B45 concrete (LSTC, 2021b).

Table 4.1 Pier material properties

Material	Density	E-modulus	Poisson's ratio	Yield stress
Concrete	2400 kg/m^3	36 GPa	0.2	45 MPa

The piers are reinforced with longitudinal and transverse steel reinforcements of diameters 30 and 20 mm, respectively. The rebars are modelled with Hughes-Liu beam elements. It is the default beam formulation in LS-Dyna and has several advantages, including:

- It is incrementally objective, meaning that rigid body rotation does not cause strains, allowing for treating finite strains that occur in many applications.
- It is simple, resulting in a low computational time and high robustness.
- It includes finite transverse strains. Additionally, the added computational time required to retain this strain component is insignificant.

The material model 024-PIEVEWISE_LINEAR_PLASTICITY was used to model the reinforcement steel. It is an elastoplastic material with arbitrary stress as a function of a strain curve, and an arbitrary strain rate dependency can be defined (LSTC, 2021b). The reinforcements are connected to the pier, as well as the pier and the pile cap by carefully modelling the reinforcement rebars such that the nodes of the pier, reinforcements, pier and pile cap are lined up and merged. The material properties of the pier rebars are shown in table 4.2, and the FEA model of the reinforcements is shown in figure 4.3. In addition to the properties below, the strain rate scaling effect on yield stress is defined using the Cowper-Symonds method with parameters C=40.4 and P=5 (Mehreganian et al., 2018).

Table 4.2 Rebars material properties

Material	Density	E-modulus	Poisson's ratio	Yield stress
Steel	7850kg/m^3	200 GPa	0.3	588 MPa

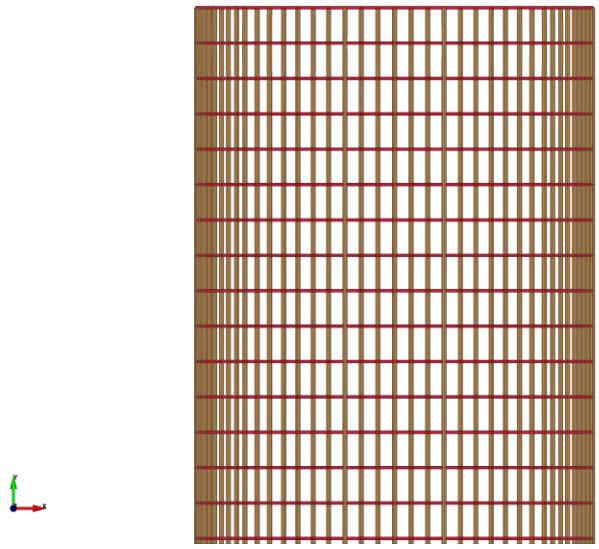

Figure 4.3 Modelling of the pier reinforcement

4.2.2. Pier and pile cap

The pier and the pile cap are massive concrete blocks connecting and transferring loads between the superstructure, bridge piers, and the foundation/soil. The pier cap has the shape of a rectangular block with length 11.4 m, width 10.9 m, and depth 2.5 m, and the pile cap has a shape resembling an inverted square frustum with upper length 13.1 m, lower length 12.3 m, width 5.7 m, and depth 3.2 m.

The meshing of the pier and the pile cap consists of variable element sizes to get a continuous mesh connection with the piers and reduce the computational cost. They are modelled with under-integrated constant stress solid elements, and the elements are assigned the same hourglass control as the solid bridge pier elements. Figure 4.4 shows the pier and the pile cap.

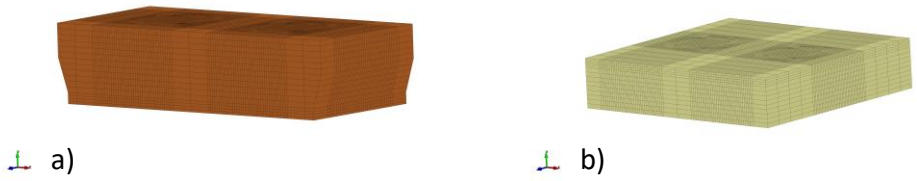

Figure 4.4 a) pier cap and b) pile cap

The concrete of the pier and the pile cap are modelled with material model *MAT_ELASTIC. The elastic material is chosen to simplify the model and reduce the computational demands of the FEA. Table 4.3 shows the material properties of the pier and the pile cap.

Table 4.3 Pier and pile cap material properties

Material	Density	E-modulus	Poisson's ratio
Concrete	2400 kg/m^3	36 GPa	0.2

4.2.3. Pile foundation

Six friction piles support the bridge piers and pile cap. The piles are tubular and have diameter 0.5 m and depth 22.3 m and are modelled with Hughes-Liu beam elements. The piles are of steel, and table 4.4 shows the material properties. The piles are inserted 0.9 m into the pile cap and are connected with the pile cap by merging the pile nodes with the pile cap nodes.

Table 4.4 Pile material properties

Material	Density p	E-modulus	Poisson's ratio
Steel	7850kg/m^3	200 GPa	0.3

The modelling of the soil-pile interaction with spring elements follows the procedure by Fan et al. (2021). The procedure uses lateral p-y springs to model the lateral soil resistance and vertical

q-z and t-z springs to model the end bearing and shaft friction, respectively. The soil-pile interaction is modelled using various nonlinear springs in the vertical and lateral directions located along the longitudinal direction of the piles. The springs are modelled as discrete elements and are defined between the pile nodes and fixed nodes in space. Each set of springs consists of five springs, one in the vertical direction and four in each lateral direction. The spring sets located along the pile length consist of four p-y springs and one t-z spring, and the spring sets located at the pile tip consist of four p-y springs and one q-z spring. Figure 4.5 shows the modelling procedure of the soil-pile interaction.

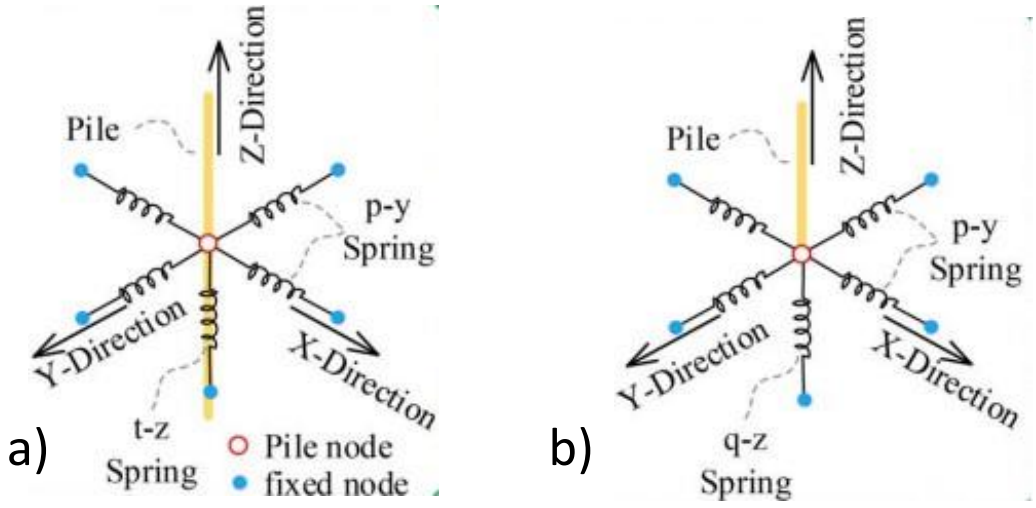

Figure 4.5 Soil-pile interaction modelling of a)springs along with the pile and b) springs at the pile tip (Wang et al., 2014)

The spring properties are determined using the API specification (API, 2007). The soil domain is taken from Wang et al. (2014), where the soil consisted of medium dense sand with a friction angle 33° and bulk density 19 kN/m^3. Appendix II shows the full calculation of the spring forces.

The lateral soil resistance is modelled with four compression-only p-y springs in the horizontal direction. To determine the lateral bearing capacity at a given depth, the smallest value of p_{us} or p_{ud} (equations 35 and 36) should be considered the ultimate bearing capacity.

$$p_{us} = (C_1 * H + C_2 * D) * \gamma * H \quad (35)$$

$$p_{ud} = C_3 * D * \gamma * H \quad (36)$$

where

- p_u: Ultimate bearing resistance at depth H
- γ: Effective soil weight
- H: Depth
- C_1, C_2 and C_3 are determined from figures in the API specification (2007, p. 70), and is a function of the angle of internal friction
- D: Pile diameter

(API, 2007)

To simplify the modelling of the p-y springs, the ultimate bearing capacity p_u is determined at depth 11.15 m, which is half of the total pile depth. After the ultimate lateral soil resistance is determined, equation 37 can be used to determine the load-deflection relationship for the p-y springs (API, 2007, p. 70).

$$P = A * p_u * \tanh\left(\frac{k * H}{A * p_u}\right) * y \quad (37)$$

where

- A: factor to account for cyclic or static loading conditions, and is taken as 0.9
- k: Initial modulus of subgrade reaction, and is determined from figures in the API specification (2007, p. 70) and is a function of the relative density
- y: Lateral deflection

Equations 38 and 39 are used to determine the values for the shaft friction f and unit end bearing q, which are used to determine the properties of the q-z and t-z springs.

$$f = \beta * p_o' \quad (38)$$

$$q = N_q * p_o' \quad (39)$$

where

- β: Dimensionless shaft friction factor
- N_q: Dimensionless bearing capacity factor
- p_o': Effective overburden pressure

The shaft friction and unit end bearing may not increase linearly with the overburden pressure for long piles. Because of this, the API specification recommends limiting values for the shaft friction f and unit end bearing q equal to 81kPa and 5MPa, respectively (API, 2007, p. 64).

After the shaft friction and unit end bearing are determined, the load-deflection relationship curves for the q-z and t-z springs are determined using specific tables in the API specification (API, 2007, pp. 66-68).

Pile group effect

According to the API specification (2007, p. 71), pile groups embedded in either cohesive or cohesionless soils and subjected to lateral loads will experience more significant deflections than a single pile under the average pile load corresponding group. This effect is called the pile group effect and is modelled by modifying the incorporating P-multipliers into the properties of the p-y springs. Each pile is assigned a P-multiplier based on the pile diameter and spacing and the pile location within the pile group and follows the procedure in the AASHTO Bridge Design Specification (2012, pp. 10.77-10.88). Figure 4.6 shows the different P-multipliers based on the pile location.

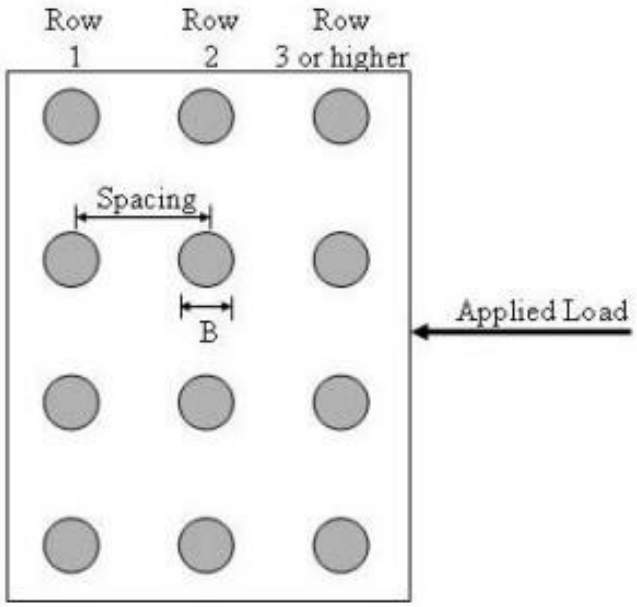

	Row 1	Row 2	Row 3
P-multiplier	1	0.85	0.7

Figure 4.6 Pile group effect according to AASHTO (2012)

Gap effect

MAT_SPRING_INELASTIC (MAT_S08) and MAT_SPRING_GENERAL_NONLINEAR (MAT_06) are the spring materials used in the LS-DYNA model) to represent the nonlinear behaviour of the piles and the soil-pile interaction (Fan et al., 2021). However, when a pile is subjected to large lateral loads, the soil develops gaps at the soil-pile boundary due to permanent soil deformation (Consolazio et al., 2003). As we can see from the work of Fan et al. (2021), MAT_08 can capture the gap effect, and MAT_S06 cannot, which makes MAT_08 preferable when modelling the lateral p-y springs. Because of this, MAT_08 is used to model the horizontal p-y springs, while MAT_S06 is used to model the vertical q-z and t-z springs.

4.3. The global model

A simplified, global FE model of a bridge (excluding the local model) is modelled to complement the local bridge model to analyse the global response of a bridge subjected to a ship collision. The global bridge model includes the bridge deck, two bridge piers, two pier caps, and bearings and is modelled with Hughes-Liu beam elements. The bridge deck is modelled with longitudinal and transverse beams. The longitudinal beams are modelled with rigid material (*MAT_RIGID) to avoid buckling after the impact, while the transverse beams are modelled with elastic material (*MAT_ELASTIC). The simplified pier caps and bridge piers of the global model are modelled with elastic beams. The global bridge model materials has modulus of elasticity 36 GPa and Poisson's ratio 0.2

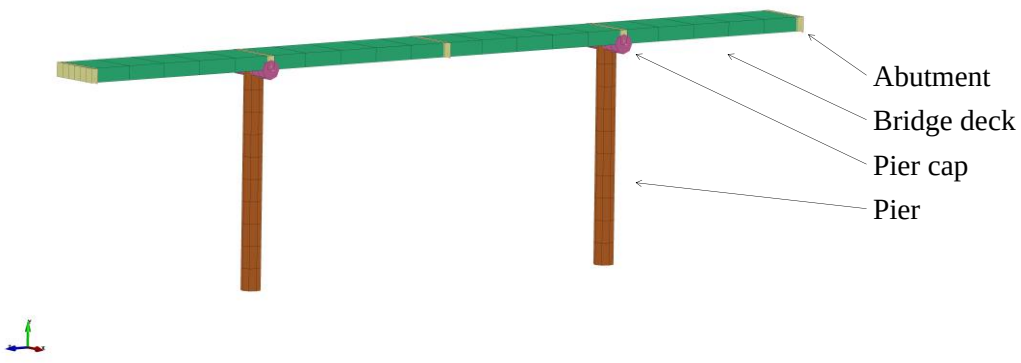

Figure 4.7 The global sub-model

The mass of the bridge deck is 4000 t, and the mass of the global piers and pier caps are 775 t and 553 t, respectively. The mass of each global pier and pier cap are equal to the mass of the pair of bridge piers and the pier cap of the local model, respectively, such that one pier of the global model has a mass equal to the local pair of piers, and one pier cap of the global model has mass equal to the local pier cap.

Elastomeric bearings are used to connect the pier caps and bridge deck and transfer both the vertical and lateral loads from the piers to the superstructure. The bearings are modelled with discrete elements. Four bearings were used above each pile cap. Each bearing is modelled with 3 springs (one in each horizontal direction and one in the vertical direction) and 3 dampers in the same directions. The springs are two-way elastic springs modelled with the keyword *MAT_SPRING_ELASTIC in LS-Dyna, and the dampers are modelled with the keyword *MAT_DAMPER_VISCOUS. The stiffness for a single vertical bearing is taken as $1.87*10^{10}$ N/m, and the stiffness for a single horizontal bearing is taken as 2.33*10^7 N/m, and the damping ratio is taken as 0.14 for both the vertical and horizontal bearings (Bi et al., 2013).

4.4. The ship model

The FE ship bulb model is an imported LS-Dyna model I got from my supervisor, Professor Yanyan Sha. The ship bulb model initially had a mass equal to 64 t. However, for the ship bulb model to resemble an entire ship and not just a ship bulb, the ship bulb model was modified to have increased mass (between 1000 t and 4000 t), depending on the impact conditions that was to be simulated. The ship is placed as close to the bridge model as possible, such that the impact happens as soon as the initial velocity is applied to the ship.

The ship bulb model consists of Belytschko-Tsay shell element. It uses a co-rotational stress update instead of the costly Jaumann stress rotation used for the Hughes-Liu shells (LSTC, 2006). Because of this, the Belytschko-Tsay shell type is more economical than the Hughes-Liu shell type, at the cost of accuracy, especially if the shell nodal points are co-planar (Galbraith & Hallquist, 1995). The shells are defined with two through shell thickness integration points.

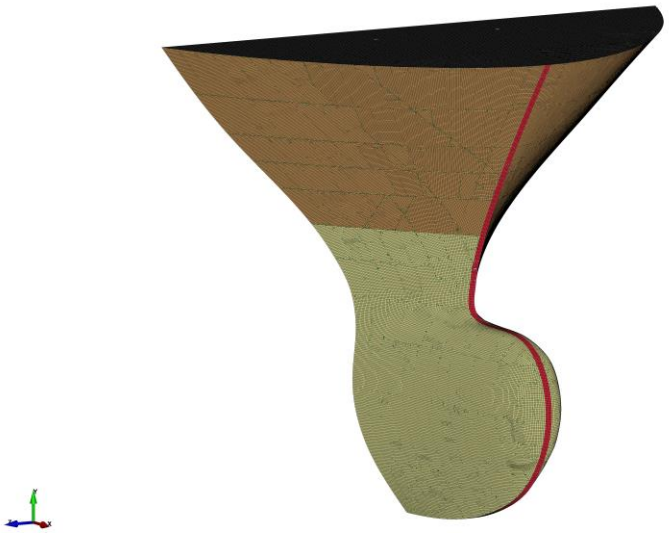

Figure 4.8 The ship bulb model

The material of the ship bulb is exclusively steel and is modelled with the keyword MAT_PIECEWISE_LINEAR_PLASTICITY. Table 4.5 shows the material properties of the ship model. In addition to the properties below, the strain rate scaling effect on yield stress is defined using a previously developed ship model provided by my supervisor Yanyan Sha.

Table 4.5 Ship material properties

Material	Density	E-modulus	Poisson's ratio	Yield stress
Steel	7800kg/m^3	200 GPa	0.3	275 MPa

The ship is applied an initial velocity with the LS-Dyna keyword *INITIAL_VELOCITY_GENERATION, which acts as the impact velocity. With this keyword, velocity can be applied in the specified direction. The velocity can also be defined to be applied at a specific time in the simulation using the keyword *INITIAL_VELOCITY_GENERATION_START_TIME.

4.5. Boundaries, constraints, and contact formulations in the FE model

The boundaries of the FE model are modelled using the LS-Dyna keyword *BOUNDARY_SPC_SET. This is used to model the following boundaries:

- Fix the nodes in space that are connected to the springs. This applies to the spring nodes for the soil-pile interaction modelling (local model) and the spring nodes for the bearing modelling (global model).
- Fix the nodes at both ends of the global bridge model to model the abutments at each end.
- Fix the global, simplified piers at the bottom node.

The constraints are modelled using the LS-Dyna keyword *CONSTRAINED_NODAL_RIGID_BODY_SPC. It is used to constrain all the nodes at the back of the ship model to a node located at the centre of the nodal rigid body and constrain all nodes in all directions, except in the horizontal directions to enable horizontal motion of the ship.

To address self-contact between the elements sharing the same surface, the single surface contact formulation *CONTACT_AUTOMATIC_SINGLE_SURFACE is used. It is a surface contact formulation that considers the self-contact between all slave surfaces and is discussed in chapter 3.2.11. The keyword is used for both the self-contact formulation of the bridge model and the local pier model, and no master surface is defined for this contact formulation. For the ship model, the ship model is set as slave segments, while for the local model, the bridge piers (including the reinforcements), and the pier and the pile cap are set as slave segments. For both cases, the static and dynamic coefficients of friction are 0.2.

The contact modelling for the impact between the ship and the bridge piers is defined using the contact treatment *CONTACT_AUTOMATIC_SURFACE_TO_SURFACE. This is a two-way treatment of contact and is discussed in chapter 3.2.11. The ship model is divided into two segments, one upper and one lower segment, and contact is defined as the impact between both the lower ship segment and the impacted pier and the upper ship segment and the impacted pier. The ship segments are slave segments, while the impacted pier (including the reinforcements), and the pier and the pile cap are master segments. As with the self-contact formulation, the static and dynamic friction coefficients are 0.2.

4.6. Gravity

Gravity load is applied to the bridge model with the LS-Dyna keywords *LOAD_BODY_Y and *LOAD_BODY_PARTS. Initially, the plan was to add dynamical gravity relaxation to preload the gravity load before the regular analysis, in order to apply the gravity load to the structure without adding KE to the system. However, as this caused significantly increased computational cost, the dynamic relaxation of the gravity was disregarded. To reduce the effect of gravity on the system's energy, the ship's initial velocity is applied 0.5 seconds after the gravity load is applied. During the initial 0.5 seconds, the model is applied heavy damping to reduce the KE arising from the application of the gravity load. Figure 4.9 shows the time history of the energy balance of the FE system when applying heavy damping for the first 0.5 seconds before applying the initial velocity to the striking ship. As the total energy is consistently 50 MJ after the initial velocity is applied, the gravity load applies an insignificant amount of KE to the system.

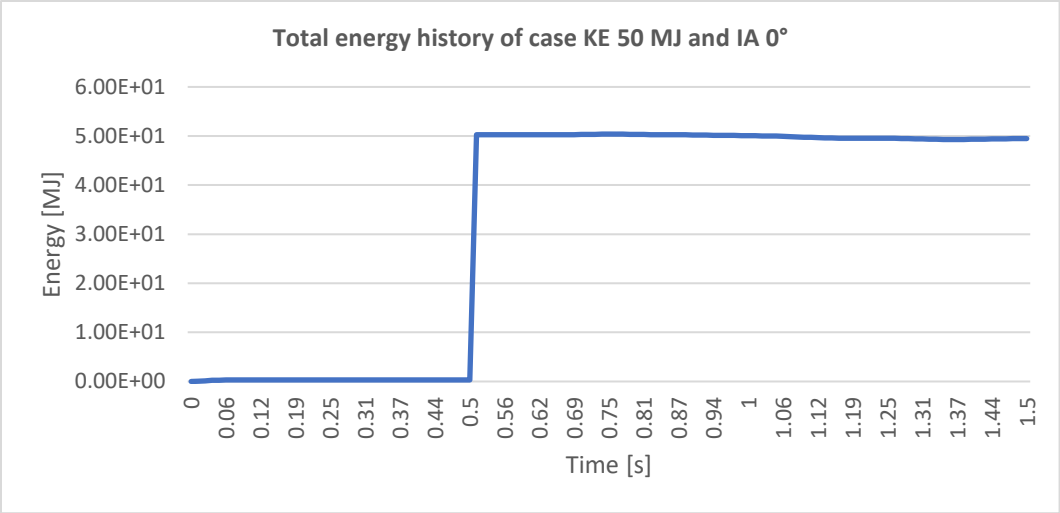

Figure 4.9 Total energy with heavy initial damping

4.7. FEA with LS-Dyna

A dynamic, explicit FE analysis in LS-Dyna is performed to analyse the ship-bridge collision with the half-step central difference scheme discussed in chapter 3.2.4 (LSTC, n.d.-g).

Due computational time required to perform the FEA, an MPP (Massively Parallel Processing) solver in LS-Dyna is used. The MPP solver uses HPC (High Performance Computing) to reduce

the simulation time required for the analysis. According to Oasis (2018), "it uses a message passing protocol to exchange information between the cores on a board or over a network". The solver decomposes the domain of the problem and distributes it to different cores using MPI (Message Passing Interface) protocols to communicate between the subdomains (Oasis, 2018).

A significant advantage of the MPP solver is that the MPP solver can use several computers connected in a network, compared to the SMP (Shared Memory Parallel) solver, which only uses a single computer. Additionally, the MPP solver is scalable for over 16 CPUs, while the SMP solver is only scalable for up to 8 CPUs (Oasis, 2018). These advantages drastically reduce the simulation time required for the analysis.

4.7.1. Analysis parameters

The analysis will include numerous simulations with different impact conditions related to the impact speed, ship mass, and impact angle to study how the Heinrich factor is related to the different impact conditions for the particular bridge model used in this study.

- The first set of simulations will be head-on collisions (impact angle 0°) with different impact speed and ship mass, with impact speeds of 3, 4, and 5 m/s and ship masses of 1000, 2000, 3000, and 4000 t.
- The second set of simulations will be with varying KE (which depends on the ship velocity and ship mass with the formula $E_k = \frac{1}{2}mv^2$) and impact angle, with KEs 24, 32, 37.5, and 50 MJ and impact angles 0°, 15°, 30°, 45°, 60°, and 90°.

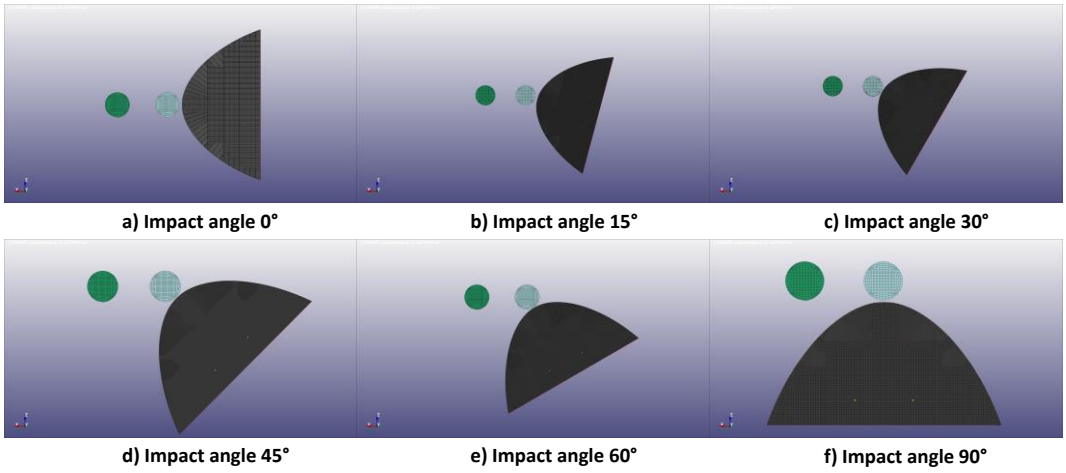

Figure 4.10 Angles in simulation set two

Simulation set one included 12 simulations, and simulation set two included 20 simulations. Initially, the plan was to include cases with an impact speed 2 m/s, but due to insignificant deformation and minimal chance of collapse for the cases of impact speed 3 m/s, simulations with impact speed 2 m/s are excluded in the study.

The simulation run time depends on the impact velocity. The simulation terminates when the ship has moved 5 m with the initial velocity (ignoring collision). E.g., for an impact velocity 5 m/s, the termination time is set to 1.5 s (0.5 s is added to the simulation time, because the initial velocity of the ship is applied after 0.5s). For impact velocity 4 m/s, termination time was set to 1.75 s, and for impact velocity 3 m/s, termination time was set to 2.17 s.

Based on observations of the simulation results, a strong correlation between the displacement of the impacted bridge pier and the amount of damage from the impact was observed. Because of this, the peak displacement of the impacted pier is recorded and used to determine the Heinrich Factor.

The simulation results are presented and analysed in chapter 5. The method for determining the Heinrich Factor based on the lateral deflection of the impacted pier is proposed in chapter 6.

5. Results

5.1. Collapse determination

After performing the simulations, the simulation results are observed and analysed, and an assessment of each simulation result is made regarding whether the impacted bridge pier collapses or not. It is assumed that the impacted pier collapses if it fractures after the impact. Figure 5.1 shows the simulation result for the case of KE 50 MJ and impact angle 0°. Figure 5.1 shows the deformation, and figure 5.1b shows the initial fracture of the bottom part of the pier after 1.2 s.

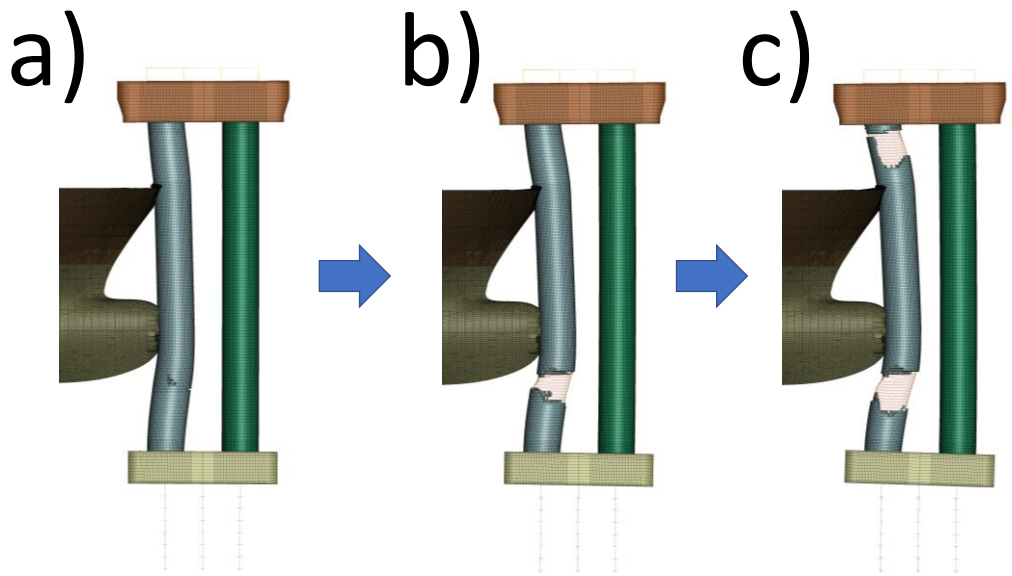

Figure 5.1 Pier response after impact for KE 50 MJ and impact angle 0° at a) t=1 s, b) t=1.2 s and c) t=1.5 s

In simulation set one, where the impact velocity and ship mass are the variables (impact angle is set to 0°), collapse can be seen in the following cases:

- Impact velocity 5 m/s and ship mass 4000 t
- Impact velocity 5 m/s and ship mass 3000 t
- Impact velocity 4 m/s and ship mass 4000 t

No collapse is seen in the other cases. I.e., all cases with KE equal to or above 32 MJ cause collapse, and cases with KE below 24 MJ do not cause collapse.

In simulation set two, where the KE of the ship and the impact angle are the variables, it was observed that the impact angle affects whether the pier collapses or not. All cases with KE 24 MJ caused no collapse, no matter the angle. For KE 32 MJ, the pier collapsed for impact angles of 45° or below, and for 37.5 MJ, the pier collapsed for all impact angles of 30° or below. The assessments regarding whether the pier collapses or not is summarised in tables 5.1 and 5.2.

Table 5.1 Collapse determination for simulation set one

Ship mass (t)	Velocity (m/s)		
	3	4	5
1000	No collapse	No collapse	No collapse
2000	No collapse	No collapse	No collapse
3000	No collapse	No collapse	Collapse
4000	No collapse	Collapse	Collapse

Table 5.2 Collapse determination for simulation set two

KE	Impact angle					
	0°	15°	30°	45°	60°	90°
24	No collapse	No collapse	No collapse	No collapse	No collapse	No collapse
32	Collapse	Collapse	Collapse	Collapse	No collapse	No collapse
37.5	Collapse	Collapse	Collapse	No collapse	No collapse	No collapse
50	Collapse	Collapse	Collapse	Collapse	Collapse	Collapse

It was observed that increasing impact angle decreases the chances of collapse of the pier by observing the simulation results for the cases with KE 32 and 37.5 MJ. For the case of KE 32 MJ, the collapse was observed for the impact angles 60° and 90°, while for the case of KE 37.5 MJ, the collapse was observed for the impact angles 45°, 60°, and 90°. The increased impact angle decreases the chance of collapse of the pier, and follows the theory of Jensen (2017) discussed in chapter 3.1.3, which states that a head-on collision will have the most collision energy and that the collision energy will decrease with increasing impact angle.

Interestingly, the pier collapses for KE 32 MJ and impact angle 45°, while it does not collapse for KE 37.5 MJ and 45° impact angle. This was an unexpected result, as the ship collision

impact action is characterised by the KE of the striking vessel, as mentioned in chapter 3.1.5. The impact conditions for KE 32 MJ is impact velocity 4 m/s and ship mass 4000 t, and the impact conditions for KE 37.5 MJ is impact velocity of 5 m/s and ship mass 3000 t. Based on this information, the ship mass is of greater significance on whether the pier collapses or not, compared to the significance of ship mass on the KE with the KE formula in equation 15.

5.2. Energy dissipation

For all cases, most of the KE becomes internal strain energy, and the rest remains as KE, or becomes spring and damper energy, sliding interface energy, hourglass energy, and eroded energy. Figure 5.2 shows the balance between the kinetic and internal energies for the case of KE 50 MJ and impact angle 0°. Interestingly, the dissipation of the KE to internal strain energy is unaffected by the impact angle. For all cases, around 80% of the KE is converted to internal energy, and around 2.5% of the initial KE remains as K, when measured at the end of the simulation (the simulation time is discussed in chapter 4.7.1). Table 5.3 shows the other types of energy the initial KE becomes, as well as the external work for the case of KE 50 MJ and impact angle 60°, measured at the end of the simulation. Note that the total energy is the sum of the internal, kinetic, sliding interface, hourglass and system damping energy (LSTC, n.d.-h).

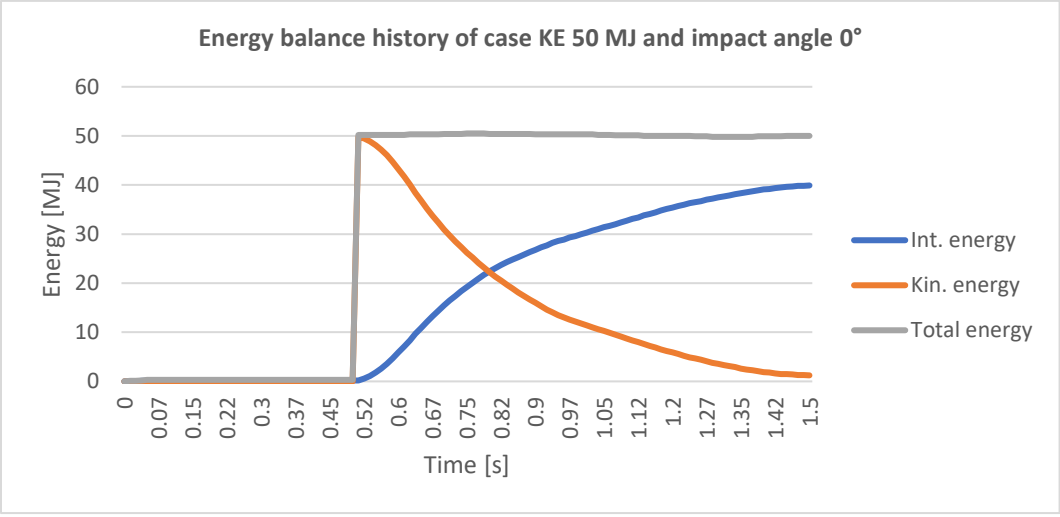

Figure 5.2 Total, kinetic and internal energy of case KE 50 MJ and impact angle 0°

Table 5.3 Energy balance of case KE 50 MJ and impact angle 60°

Energy type	Energy amount (in MJ)
Total energy	50
KE	1.22
Internal energy	39.9
Spring and damper energy	1.62
Hourglass energy	0.85
System damping energy	6.13
Sliding interface energy	1.93
External work	0.08
Eroded KE	0.05
Eroded internal energy	5.36
Eroded hourglass energy	0.17

5.3. Section forces and moments

When observing the simulation results for the cases causing collapse, the impacted pier first fractures in the bottom part, as shown in figure 5.1. The failure mode resembles a combined flexural shear with the formation of a plastic hinge, pictured in figure 3.6d. The internal forces and moments of a cross-section located close to the initial failure are measured for all cases and may indicate whether the pier fails or not. Figure 5.3 shows the location of the specified cross-section.

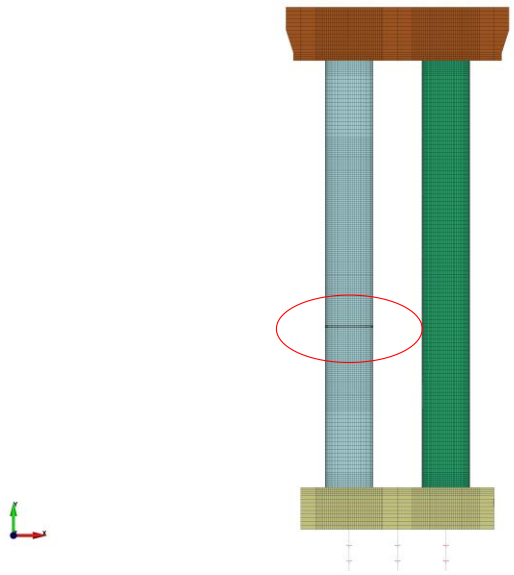

Figure 5.3 The specified cross-section

From observing internal forces and moments in the specified cross-section, the internal forces and moments of the cross-section are not affected by the increased impact energy of the collision, and the internal forces and moments were measured at 37100 kN and 41000 kNm, respectively. The internal forces and moments for the simulation cases with KEs 24, 37.5, and 50 MJ with impact angle 0% are shown in figures 5.4 and 5.5, respectively. Even though the pier collapses for the cases of KEs 50 and 37.5 MJ and does not collapse for the case of KE 24 MJ, the internal forces and moments were close to equal for all cases.

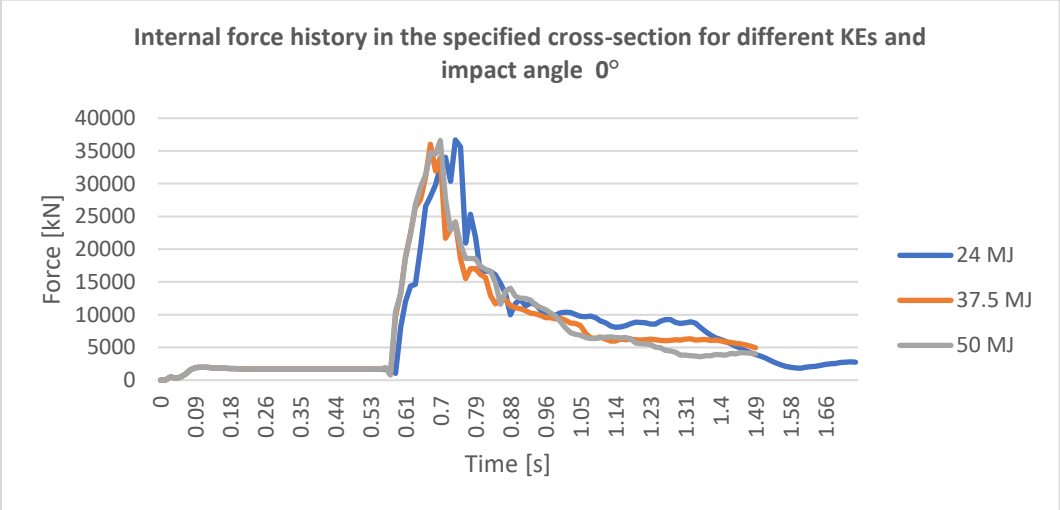

Figure 5.4 Internal forces in the specified cross-section with different KEs

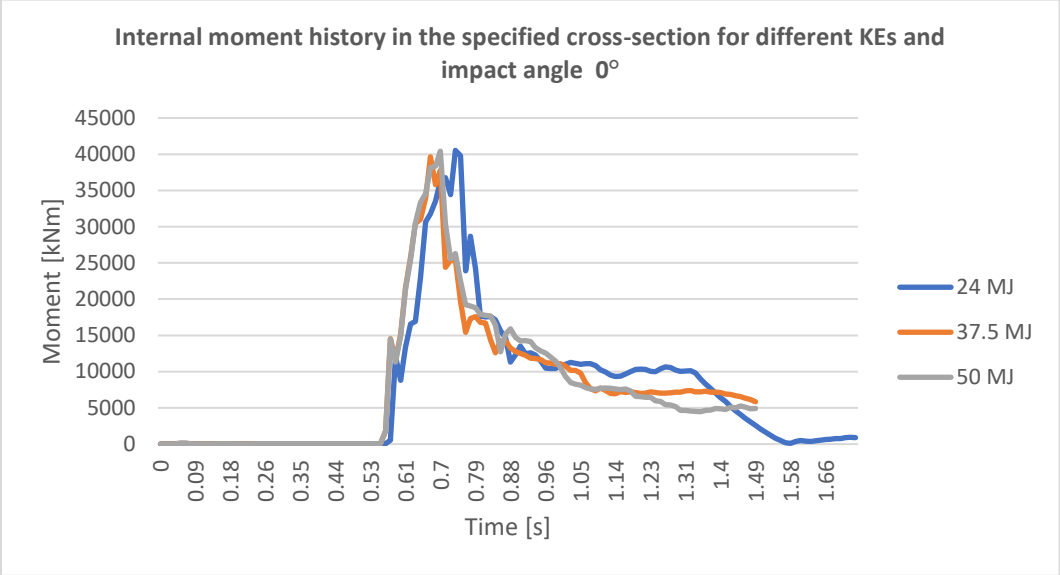

Figure 5.5 Internal moment in the specified cross-section with different KEs

However, when comparing the internal forces and moments for the cases of varying angles, instead of varying KE, a decrease in the internal force and moment with increasing impact angle is observed, and is shown in figures 5.6 and 5.7. The internal forces peak at 36600 kN for impact angle 0% and decrease to 29700 kN for impact angle 90%, and the internal moment peaks at 40400 kN for impact angle 0% and decreases to 35500 kNm for impact angle 90%. This can explain our results in chapter 5.1, where an increased impact angle caused no collapse for the KEs 32 and 37.5 MJ, while the pier collapsed for lower impact angles.

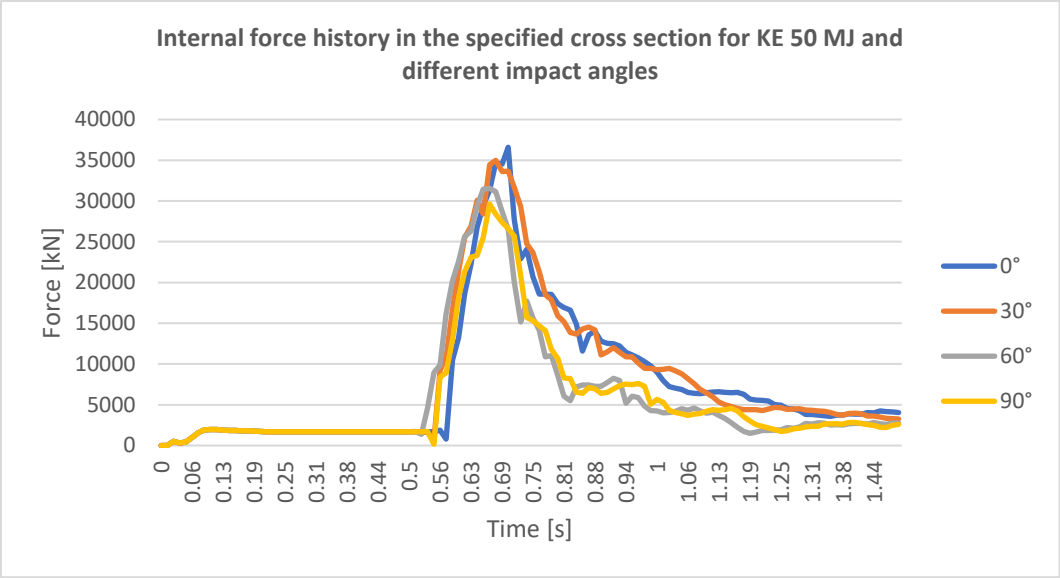

Figure 5.6 Internal forces in the specified cross-section with different impact angles

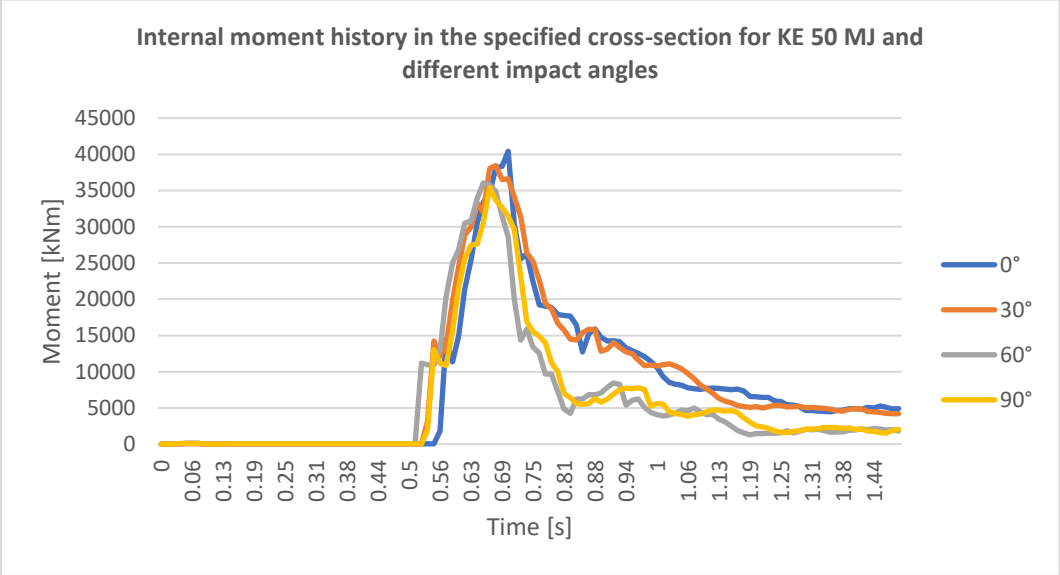

Figure 5.7 Internal moment in the specified cross-section with different impact angles

5.4. Lateral displacement

In addition to the energy balance and the section forces and moments, the resultant displacements in the horizontal directions of the impacted bridge pier were measured. It is observed that the measured displacement of the pier increases with increasing impact velocity and ship mass after the impact, as expected. The time histories for the displacements for the cases in the simulation set one with impact velocity versus ship mass are shown in figures 5.8,

5.9, and 5.10. Additionally, an overview of the peak displacements of the impacted pier for the first simulation set is shown in table 5.4.

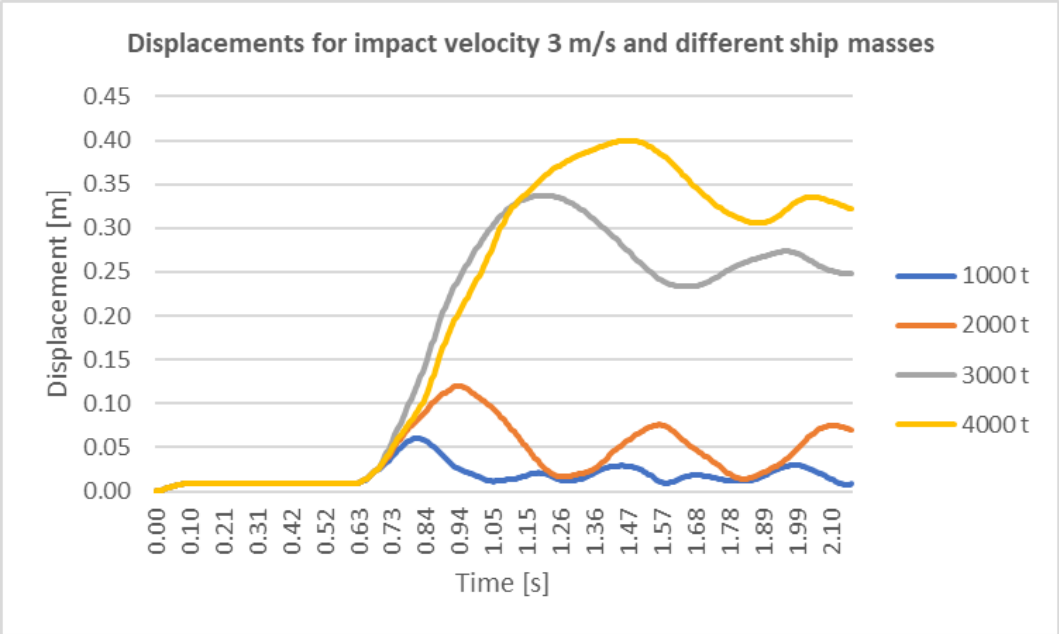

Figure 5.8 Lateral displacements of pier for impact velocity 3 m/s

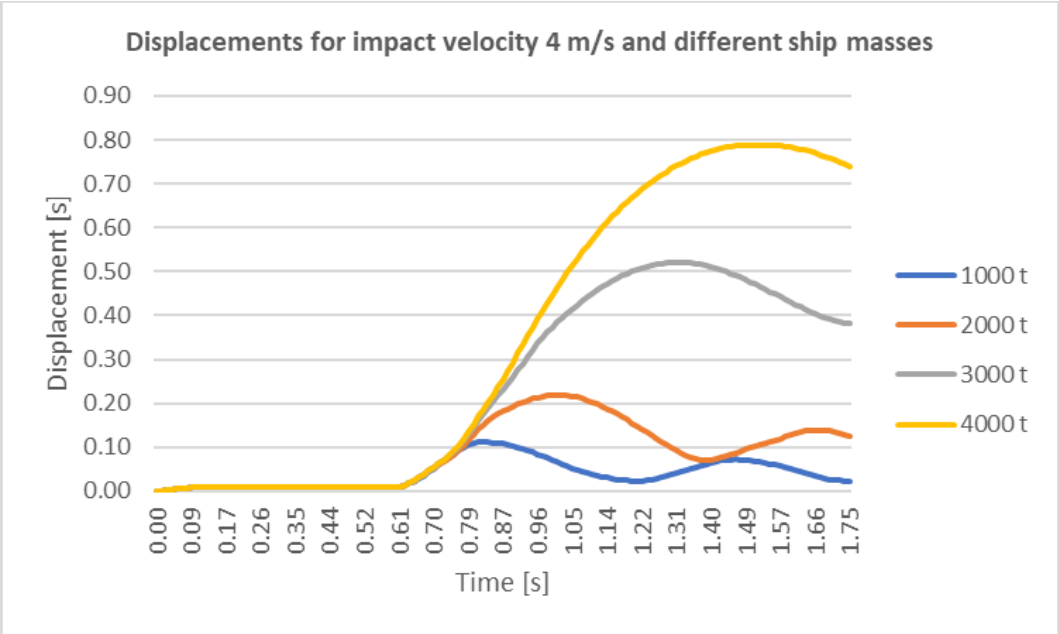

Figure 5.9 Lateral displacements of pier for impact velocity 4 m/s

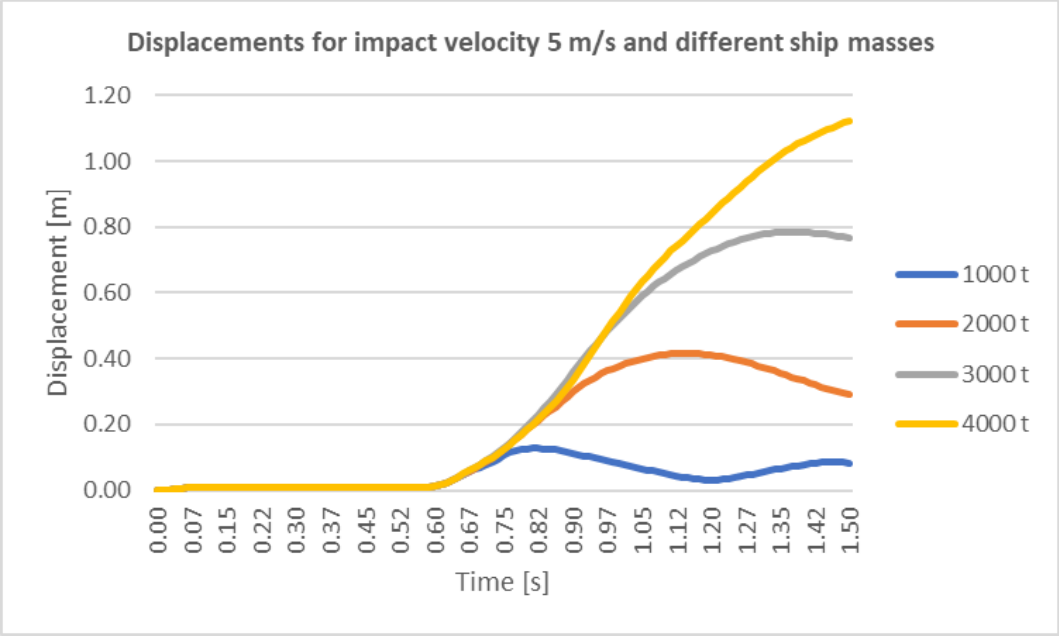

Figure 5.10 Lateral displacements of pier for impact velocity 5 m/s

Table 5.4 Overview of the peak displacements from simulation set one

Ship mass (t)	Velocity (m/s)		
	3	4	5
1000	0.06	0.11	0.13
2000	0.12	0.22	0.42
3000	0.34	0.52	0.78
4000	0.4	0.79	1.12

Note: Displacements in meters

The time histories for the impacted pier displacement for simulation set two (KE and impact angle as variables) are plotted just as for simulation set one, and the results for KEs 50 and 37.5 MJ and impact angles 0°, 30°, 60°, and 90° are shown in figures 5.11 and 5.12. Table 5.5 shows an overview of the peak displacements for simulation set two.

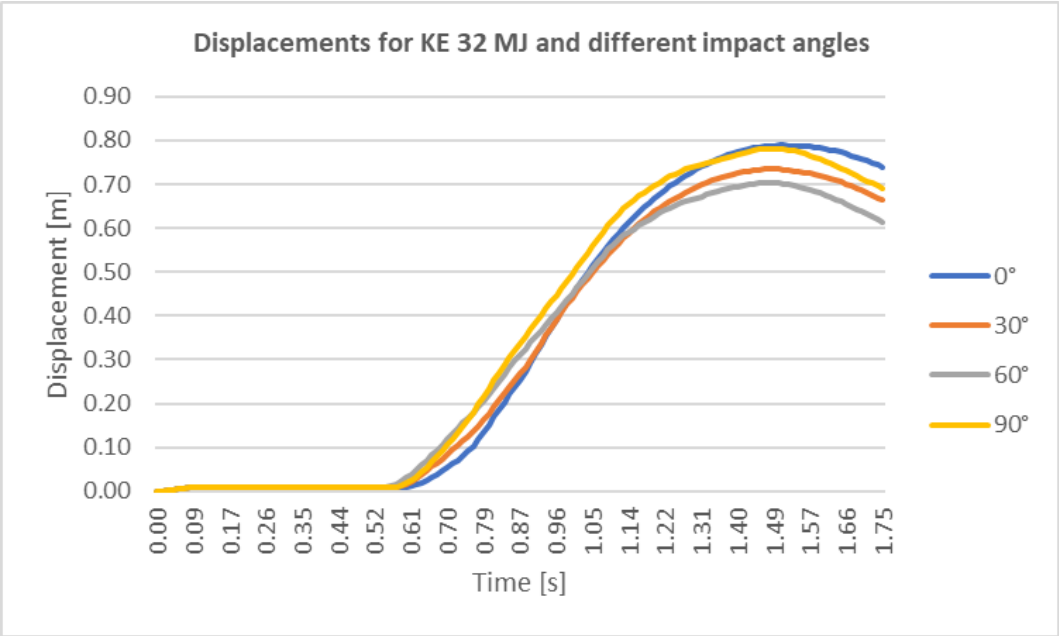

Figure 5.11 Lateral displacements of impacted pier for KE 32 MJ

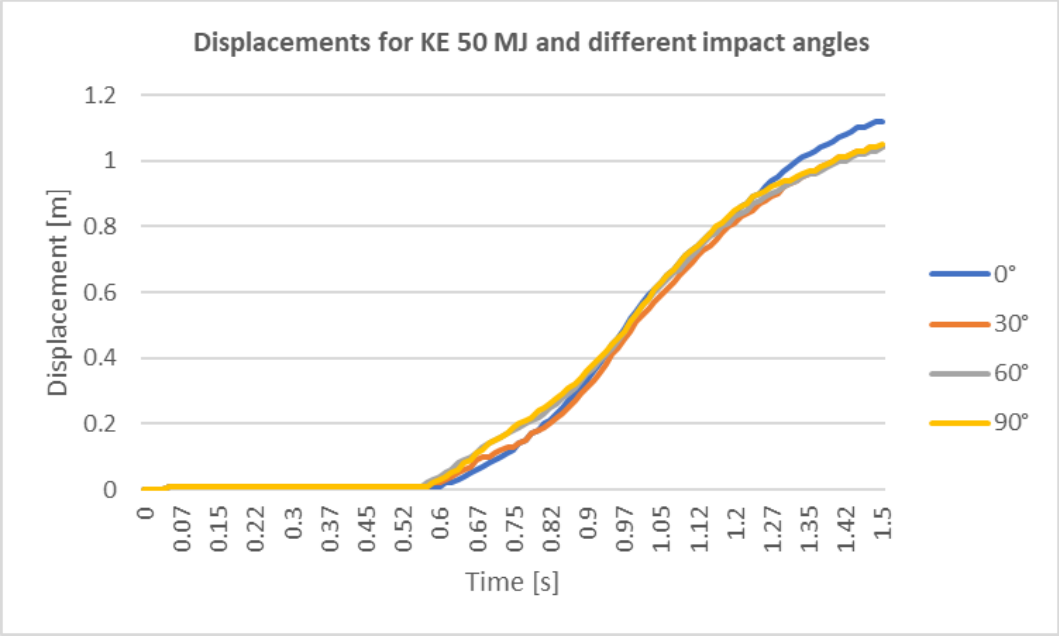

Figure 5.12 Displacements of impacted pier for KE 50 MJ

Table 5.5 Overview of the peak displacements from simulation set two

KE (MJ)	Impact angle					
	0°	15°	30°	45°	60°	90°
24	0.52	0.49	0.46	0.44	0.44	0.52
32	0.79	0.8	0.73	0.71	0.7	0.7
37.5	0.78	0.81	0.74	0.64	0.66	0.7
50	1.12	1.15	1.04	1.03	1.04	1.05

Note: Displacements in meters

6. Discussion

6.1. Collapse/no collapse determination

When comparing the displacements in tables 5.4 and 5.5 with the collapse/no collapse assessment in tables 5.1 and 5.2, a strong correlation between the peak displacements of the impacted bridge pier and whether the pier collapses or not is seen. Based on that, it makes sense to use the resultant displacement of the impacted bridge pier as a metric for determining whether the impacted bridge pier fails or not. It can be seen that in all cases, the pier collapses if the displacement of the pier exceeds 0.7 m. Therefore, the criterion for collapse is set at a displacement equal to 0.7 m, meaning that displacements above 0.7 m cause collapse and displacements equal to or below 0.7 m cause no collapse.

$$if\ lateral\ deflection > 0.7\ m \quad \rightarrow Collapse \qquad (40)$$

$$if\ lateral\ deflection \leq 0.7\ m \quad \rightarrow No\ collapse$$

Instead of using the displacement of the impacted bridge pier as the metric to decide whether the pier collapses or not, the Drift Ratio (DR) is used. It is defined as the ratio of the maximum lateral drift (displacement) to the height of the specimen, and the DR expression is shown in equation 41. The DR is a more generalised and accurate indicator of collapse than the displacement, as it considers the pier displacement relative to the pier height. Therefore, the DR will be used instead of the displacement to determine whether the pier collapses or not. Equation 42 shows the process of calculating the new criteria based on the DR, and the new criteria regarding whether the pier collapses or not is shown below equation 42.

$$DR\ (Drift\ Ratio) = \frac{lateral\ displacement}{pier\ height} \qquad (41)$$

$$New\ criteria = \frac{lateral\ displacement}{pier\ height} = \frac{0.7}{25.2} = 2.8\% \qquad (42)$$

$$if\ DR > 2.8\% \quad \rightarrow Collapse$$

$$if\ DR \leq 2.8\% \quad \rightarrow No\ collapse$$

The criteria above make sense from a logical standpoint. For the case of impact velocity 4 m/s and ship mass 3000 t with displacement 0.52 m (DR=2.06%), the pier deforms significantly, but does not fracture. Therefore, it is assumed to not collapse according to the collapse

definition in chapter 5.1, and it makes sense to define the collapse criterion above DR=2.06%. Figure 6.1 shows the response of the impacted pier for this particular case. However, for the case of impact velocity 4 m/s and ship mass 4000 t with displacement 0.79 m (DR=3.13%), the impacted bridge pier fractures. It is therefore assumed to collapse, and it makes sense to define the collapse criterion below DR=3.13%. Figure 6.2 shows the response of the impacted pier for this particular case.

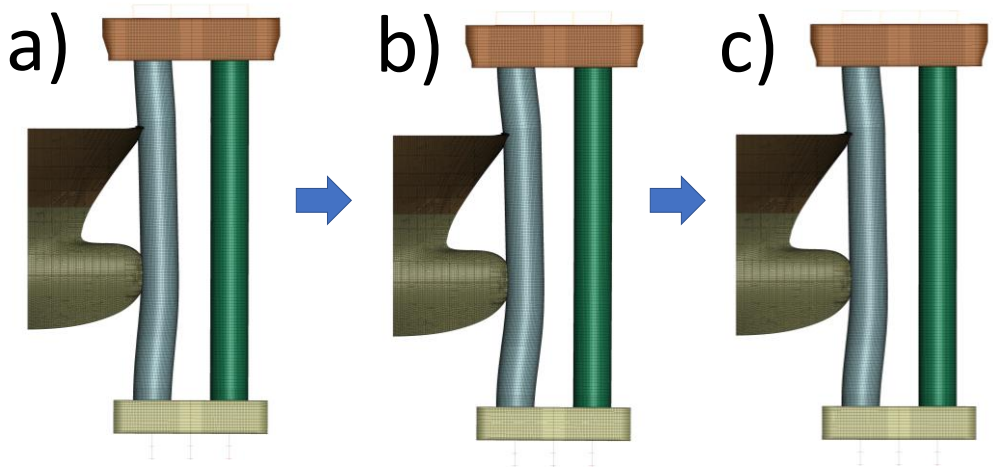

Figure 6.1 Pier response after impact for impact velocity 4 m/s and ship mass 3000 t at a) t=1 s, b) t=1.4 s and c) t=1.75 s

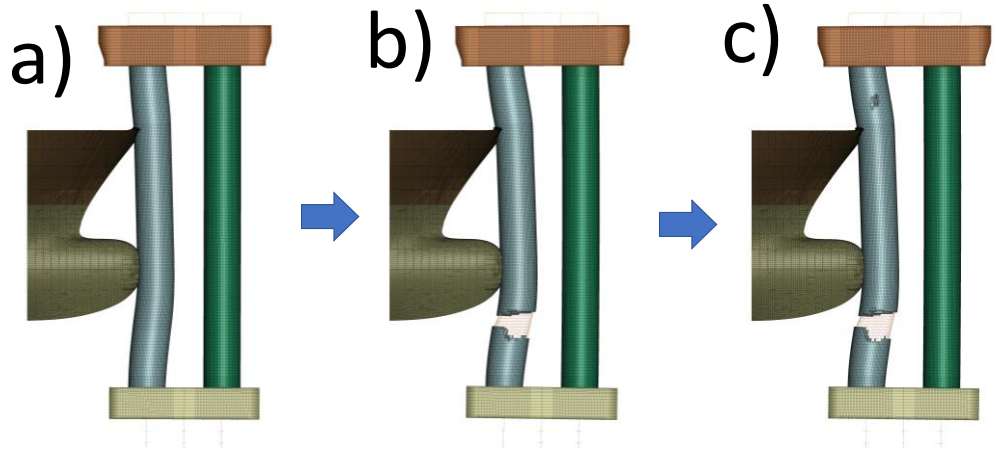

Figure 6.2 Pier response after impact for impact velocity 4 m/s and ship mass 4000 t at a) t=1 s, b) t=1.4 s and c) t=1.75 s

Using the established criteria related to DR to determine whether the impacted bridge pier collapses, tables 6.1 and 6.2 summarise which cases will cause collapse and which cases will not collapse.

Table 6.1 Collapse determination based on the criteria for simulation set one

Ship mass (t)	Velocity (m/s)		
	3	4	5
1000	No collapse	No collapse	No collapse
2000	No collapse	No collapse	No collapse
3000	No collapse	No collapse	Collapse
4000	No collapse	Collapse	Collapse

Table 6.2 Collapse determination based on the criteria for simulation set two

KE (MJ	Impact angle					
	0°	15°	30°	45°	60°	90°
24	No collapse	No collapse	No collapse	No collapse	No collapse	No collapse
32	Collapse	Collapse	Collapse	Collapse	No collapse	No collapse
37.5	Collapse	Collapse	Collapse	No collapse	No collapse	No collapse
50	Collapse	Collapse	Collapse	Collapse	Collapse	Collapse

6.2. Determination of Heinrich Factor

Instead of determining the collapse/no collapse of a bridge pier subjected to ship collision, it is more valuable to find the Heinrich Factor for the impacted pier. A criterion for the minimum DR that can cause collapse is determined by studying the simulation results. The criterion regarding the minimum DR can be used to define which cases that can cause collapse and which cases that cannot cause collapse. From observing the results of the simulation set, minimal deformations in the pier is observed for the following cases:

- Impact velocity 3 m/s and ship mass 1000 t
- Impact velocity 3 m/s and ship mass 2000 t
- Impact velocity 4 m/s and ship mass 1000 t

These cases are defined as not having the capacity to cause large enough displacements to cause the collapse of the pier. The cases all have KE below 10 MJ and caused less than 0.15 m displacement in the pier, or less than DR 0.60%. To stay conservative, the lower criterion for displacements causing collapse is set as DR 0.50%.

$$if\ DR \leq 0.50\% \rightarrow 0\%\ probability\ of\ collapse \tag{43}$$

A criterion for the required displacement to 100% cause collapse can be determined by observing the case of KE 50 MJ (impact velocity 5 m/s and ship mass 4000 t) and impact angle 0%, where extensive deformation and failure of the pier are observed. This case had pier displacement equal to 1.12 m or DR 4.4%. To stay conservative, the upper criterion for DR with 100% probability of collapse is set to 4%.

$$if\ DR \geq 4\% \rightarrow 100\%\ probability\ of\ collapse \quad (44)$$

Using all of the defined criteria above, the collapse probability or Heinrich Factor can be related to the displacement of the impacted bridge pier with a linear function for DRs between 0.50% and 4%. Consequently, if the DR is equal to or below 0.40%, there is 0% probability of collapse, and if the DR is equal to or above 4%, there is 100% probability of collapse. The proposed relationship between the Heinrich Factor and the DR of the impacted pier is shown in figure 6.3.

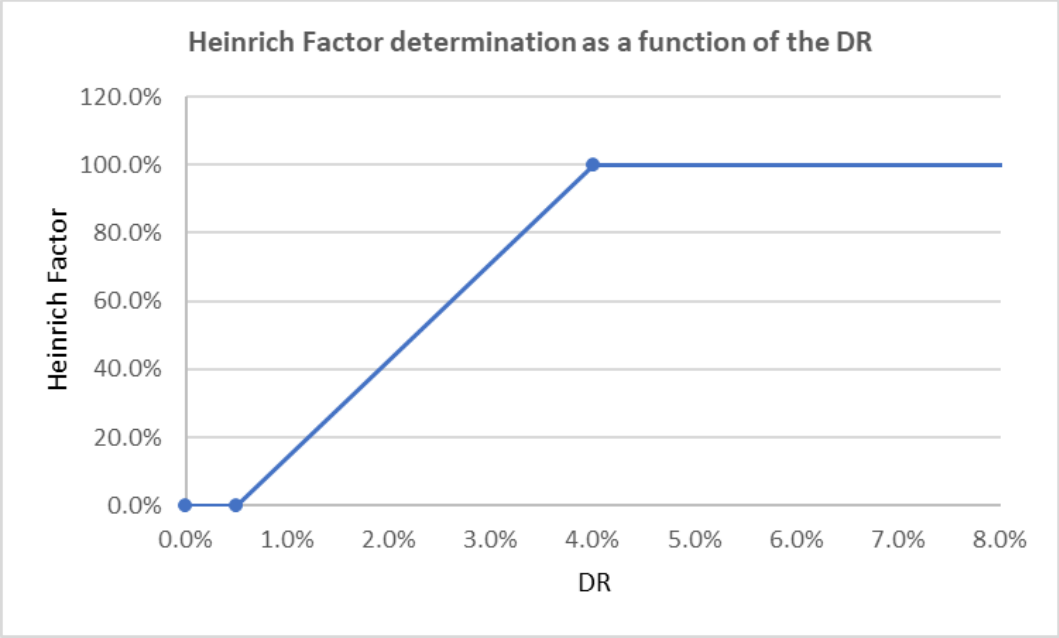

Figure 6.3 Heinrich Factor determination

6.3. Machine learning to predict collapse/no collapse

A machine learning algorithm has been developed in Python as part of this study. It uses inputs like the impact speed, ship mass, and impact angle and the simulation results in a machine learning process to estimate whether the bridge collapses or not. The determination of collapse

or no collapse is based on the DR of the impacted bridge pier, and the criteria established in chapter 6.1 decide whether the bridge collapses or not based on the peak DR of the impacted pier. The criteria are shown below.

$$if\ DR > 2.8\% \quad \rightarrow Collapse$$

$$if\ DR \leq 2.8\% \quad \rightarrow No\ collapse$$

Two Python scripts were developed to analyse the simulation results. The first Python script uses the two inputs, ship velocity and ship mass (impact angle 0°) and the collapse determination in table 5.1 as training data. The second Python script uses the two inputs, KE and impact angle, and the collapse determination in table 5.2 as training data to decide whether the pier collapses or not. Note that the scripts only work for inputs are part of the simulations, which means that the scripts does not work for other inputs (for example impact velocity 4 m/s and ship mass 4000 t works, while impact velocity 7 m/s and ship mass 6000 t does not work). The output of the scripts is a number between 0 and 1, where a number above 0.5 indicates collapse and a number below 0.5 indicates no collapse. The scripts are initiated from the Windows command prompt by selecting the correct folder and pressing 'py [scriptname].py' as shown in figure 6.4. It requires that Python is correctly installed. The scripts are shown in full in Appendix I.

$$if\ output > 0.5 \ \rightarrow Collapse$$

$$if\ output \leq 0.5 \ \rightarrow No\ collapse$$

The scripts are developed using the work of Mesquita (2021) with her permission. The first part of the scripts consists of developing the Neural Network Class for the Neural Network. The Neural Network class generates random start values from the weights and bias variables and makes an initial prediction based on the input variables before the learning process begins.

Following the creation of the Neural Network, the network must be improved by training the network with more data. To do so, the error of the first prediction is assessed, and the weight and bias variables are adjusted accordingly, such that the next prediction will be better, using the collapse/no collapse determination in tables 5.1 and 5.2 as reference. To do so, the stochastic gradient descent technique is used. It will, at every iteration, make a prediction based on some randomly selected training data, calculate the error and learn from it to get a better, more correct result for the next iteration.

The last step is defining the learning rate, defining the variables and providing the training data from the performed ship-bridge FEA simulations. This part of the code is the only part that is different between the scripts, as script one uses the simulation results from simulation set one and script two uses the simulation results from simulation set two as training data.

A couple of tests for script one were performed to control that the scripts were working as intended. First, script one is tested with an input impact velocity 5 m/s and ship mass 4000 t. According to table 5.1, this should result in collapse. Figure 6.4a shows the results, and because the output of 0.993 approaches 1, the script correctly predicts collapse. For the second test with input impact velocity 3 m/s and ship mass 3000 t, the script predicted no collapse, as the output in figure 6.4b approaches 0. Comparing the result with the collapse/no collapse determination in table 5.1, this is also a correct prediction. For these cases, 1000 iterations are performed to get the correct prediction, and for each iteration the error margin becomes smaller, as shown in figure 6.5.

The training process for script two does not work as intended due to inconsistent training data regarding the KE and impact angle that cause collapse is shown in table 5.2, and the neural network is based on a linear regression model. The inconsistency is related to the fact that the mass of the striking vessel is of greater significance on whether the pier collapses or not, compared to the significance of ship mass on the KE, and was discussed in chapter 5.1. Because of this, whether the KE is 32 or 37.5 MJ does not matter significantly because the case with KE 32 MJ has a higher ship mass (case of 32 MJ has impact velocity 4 m/s and ship mass 4000 t, while the case of 37.5 MJ has impact velocity 5 m/s and ship mass 3000 t).

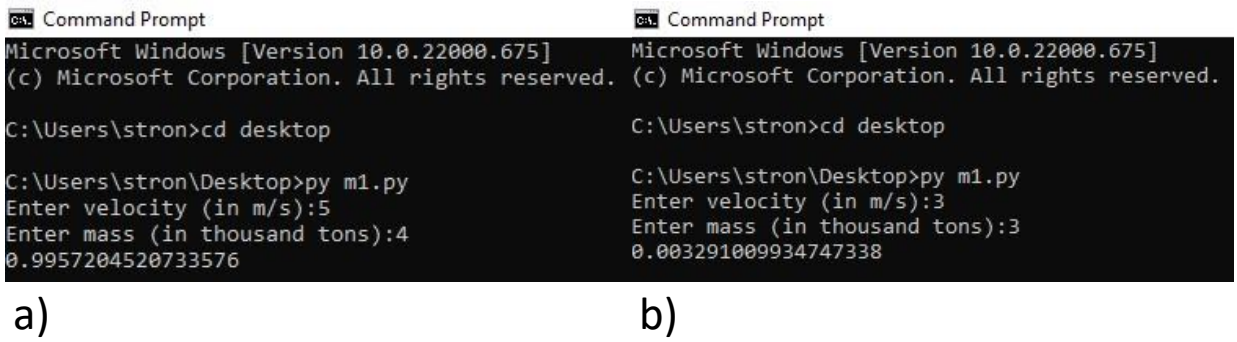

Figure 6.4 Script one machine learning predictions for a) collapse and b) no collapse

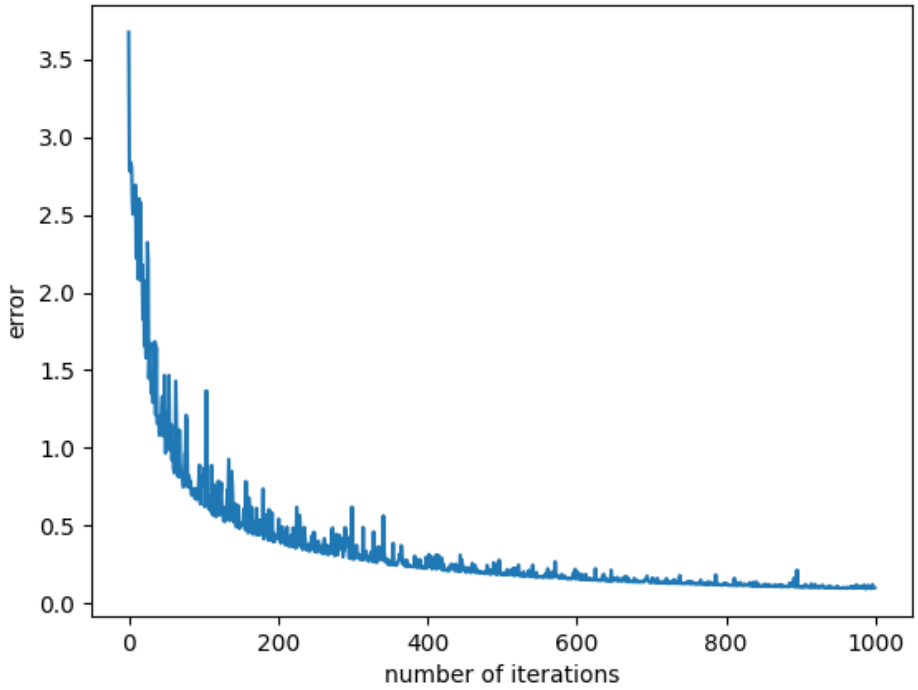

Figure 6.5 Iterative error estimation for script 1

6.4. Sources of error

Regarding the FE model and simulation results, there are some sources of error in modelling the structure. The FE model is a simplified model, and the properties and effects of the materials, geometry, contact, and boundaries are impossible to model perfectly.

Regarding the machine learning algorithm and machine learning to predict the collapse or no collapse, the training data are minimal due to only performing 32 simulations. Machine learning algorithms require much training data to function correctly, which is missing in this study. Nevertheless, the proposed procedure of using machine learning algorithms to predict the collapse/no collapse can still be used and should be able to accurately predict the collapse/no collapse with sufficient training data.

7. Conclusion

The study has conducted ship-bridge simulations, and defined a relationship between the lateral displacement of the impacted bridge pier and the Heinrich Factor. A FE model of a bridge structure is built in LS-Dyna, consisting of a local, detailed model, a less detailed global model, as well as a model of the striking ship, and the boundaries, constraints, contact and gravity are modelled carefully. 32 ship-bridge collisions using the FE model and different impact conditions related to the impact velocity, ship mass, and impact angle are simulated and analysed, and the time histories of the energy balance, internal forces and moments, and displacements were measured and compared between the different impact conditions.

A strong correlation between the amount of destruction/collapse and the lateral displacement of the impacted bridge pier was observed, and the lateral deflection, relative to the pier height (DR) was used to determine the Heinrich Factor. The relationship between the DR and Heinrich Factor are based on the established lower and upper criteria for the DR corresponding to 0% and 100% Heinrich Factor, which are conservative bounds determined from observing and analysing the simulation results. For DR's between the lower and upper criteria, a linear relationship between the DR and Heinrich Factor is defined.

Additionally, two machine learning scripts are developed in Python, which incorporate machine learning techniques to determine whether a bridge pier subjected by ship-collision collapses or not. The machine learning script uses the results from the performed simulations as training data. Based on the inputs related to the different impact conditions, the scripts determine whether the impacted bridge pier collapses or not. Script one, using input data regarding the impact velocity and ship mass function properly, while script two using input data regarding the collision energy and impact angle does not function properly due to inconsistent training data.

7.1. Further work

The FE model was developed with limited experience with the FE software LS-Dyna, and certain parts of the model are very simplified, particularly the global sub-model. Improvements in the FE model should be conducted, and the global sub-model should be modelled with less simplifications to improve the simulation accuracy and get better and more realistic results. A

higher number of simulations would also be beneficial, and would increase the accuracy of the Henrich Factor determination function based on the DR of the impacted bridge pier.

The development of the machine learning scripts in Python to predict if the pier collapses was my first coding experience, and there are many possibilities for improvement. For example, instead of the binary classification problem, where the outputs are approaches one for collapse and zero for no collapse, the output could instead be the predicted lateral deflection of the impacted pier based on the impact conditions. The predicted lateral displacements could then be used in the function for the Heinrich Factor proposed in chapter 6.2 to predict the Heinrich Factor. The possibilities are infinite!

Bibliography

AASHTO. (2009). *Guide Specification and Commentary for Vessel Collision; Design of Highway Bridges*. A. A. o. S. H. a. T. Officials.

AASHTO. (2012). *AASHTO LRFD Bridge Design specification* (Foundations, Issue. A. A. o. S. H. a. T. Officials. https://www.oaxaca.gob.mx/sinfra/wp-content/uploads/sites/14/2016/02/AASHTO-LRFD_Bridge_Design_Specifications_2010.pdf

ABS. (2021). *GUIDANCE NOTES ON NONLINEAR FINITE ELEMENT ANALYSIS OF MARINE AND OFFSHORE STRUCTURES*. A. B. o. Shipping. https://ww2.eagle.org/content/dam/eagle/rules-and-guides/current/design_and_analysis/316_gnnlfea_2021/nlfea-gn-jan21.pdf

Alrasheed, S. (2019). *Principles of Mechanics: Fundamental University Physics*. Springer International Publishing AG.

API. (2007). *Recommended Practice For Planning, Designing and Constructing Fixed Offshore Platforms*. A. P. Institute. http://icoffshore.com.vn/Uploads/files/Nghien_Cuu/TCQP/TCQT/5_API-RP-2A-WSD%20(21st%202007).pdf

Bi, K., Hao, H., & Chouw, N. (2013). 3D FEM Analysis of Pounding Response of Bridge Structures at a Canyon Site to Spatially Varying Ground Motions. *Advances in structural engineering*, *16*(4), 619-640. https://doi.org/10.1260/1369-4332.16.4.619

Buth, C. E., Williams, W. F., Brackin, M. S., Lord, D., Geedipally, S. R., & Abu-Odeh, A. Y. (2010). *Analysis of large truck collisions with bridge piers: phase 1, report of guidelines for designing bridge piers and abutments for vehicle collisions*. https://static.tti.tamu.edu/tti.tamu.edu/documents/9-4973-1.pdf

Chakrabarty, J. (2006). *Theory of plasticity* (3rd ed.). Elsevier Science & Technology.

Chen, P., Huang, Y., Mou, J., & van Gelder, P. H. A. J. M. (2019). Probabilistic risk analysis for ship-ship collision: State-of-the-art. *Safety science*, *117*, 108-122. https://doi.org/10.1016/j.ssci.2019.04.014

Consolazio, G. R., Cook, R. A., McVay, M. C., Cowan, D., Biggs, A., & Bui, L. (2006). *Barge impact testing of the St. George Island Causeway Bridge, Phase III: physical testing and data interpretation*. https://fdotwww.blob.core.windows.net/sitefinity/docs/default-source/content/structures/structuresresearchcenter/final-reports/bc354_76.pdf?sfvrsn=99eceace_0

Consolazio, G. R., & Cowan, D. R. (2003). Nonlinear analysis of barge crush behavior and its relationship to impact resistant bridge design. *Computers & structures*, *81*(8), 547-557.

Consolazio, G. R., Lehr, G. B., & McVay, M. C. (2003). Dynamic Finite Element Analysis of Vessel–Pier–Soil Interaction During Barge Impact Events. *Transportation research record*, *1849*(1), 81-90.

Cook, R. D., Malkus, D. S., Plesha, M. E., & Witt, R. J. (2002). *Concepts and applications of finite element analysis* (4th ed.). Wiley.

Fan, W., Sun, Y., Sun, W., Huang, X., & Liu, B. (2021). Effects of Corrosion and Scouring on Barge Impact Fragility of Bridge Structures Considering Nonlinear Soil–Pile Interaction. *Journal of Bridge Engineering*, *26*(8), 04021058.

Fan, W., Yuan, W., Yang, Z., & Fan, Q. (2011). Dynamic Demand of Bridge Structure Subjected to Vessel Impact Using Simplified Interaction Model. *Journal of bridge engineering*, *16*(1), 117-126. https://doi.org/10.1061/(ASCE)BE.1943-5592.0000139

Fan, W., & Yuan, W. C. (2014). Numerical simulation and analytical modeling of pile-supported structures subjected to ship collisions including soil–structure interaction. *Ocean engineering*, *91*, 11-27.

Fjær, E., Holt, R. M., Horsrud, P., Raaen, A. M., & Risnes, R. (2021). Failure mechanics. In *Developments in Petroleum Science* (Vol. 72, pp. 89-155). Elsevier. https://doi.org/https://doi.org/10.1016/B978-0-12-822195-2.00011-5

Galbraith, P. C., & Hallquist, J. O. (1995). Shell-element formulations in LS-DYNA3D: their use in the modelling of sheet-metal forming. *Journal of Materials Processing Technology*, *50*(1-4), 158-167. https://doi.org/https://doi.org/10.1016/0924-0136(94)01377-D

Garder, P. (2017). *Deficient Bridges and Safety Information*. https://utc.mit.edu/uploads/UMER25-36-Final-Report.pdf

Gardner, L., Yun, X., Fieber, A., & Macorini, L. (2019). Steel Design by Advanced Analysis: Material Modeling and Strain Limits. *Engineering*, *5*(2), 243-249. https://doi.org/https://doi.org/10.1016/j.eng.2018.11.026

Gholipour, G., Zhang, C., & Mousavi, A. A. (2018). Effects of axial load on nonlinear response of RC columns subjected to lateral impact load: Ship-pier collision. *Engineering Failure Analysis*, *91*, 397-418.

Gholipour, G., Zhang, C., & Mousavi, A. A. (2021). Nonlinear failure analysis of bridge pier subjected to vessel impact combined with blast loads. *Ocean engineering*, *234*, 109209. https://doi.org/10.1016/j.oceaneng.2021.109209

Hanses, K. (2015). *Concrete construction* (B. Bielefeld, Ed.). Birkhäuser.

Heinrich, H. W. (1959). *Industrial accident prevention : a scientific approach* (4th ed.). McGraw-Hill.

Jensen, T. K. (2017). *Bestemmelse af Heinrich-faktor i forbindelse med "Ferjefri E39"*. Rambøll.

Jernberg, A., Bhalsod, D., Zhang, G., & Blankenhorn, G. (2018). LSTC WinSuite – a complete solution for the Windows platform. *2022*(08.03).

Kh, H. M., Özakça, M., & Ekmekyapar, T. (2016). *Typical stress-strain curve for concrete*. Researchgate, A Review on Nonlinear Finite Element Analysis of Reinforced Concrete Beams Retrofitted with Fiber Reinforced Polymers. https://www.researchgate.net/publication/315716360_A_Review_on_Nonlinear_Finite_Element_Analysis_of_Reinforced_Concrete_Beams_Retrofitted_with_Fiber_Reinforced_Polymers

Kim, N.-H. (2015). Finite Element Analysis for Contact Problems. In *Introduction to Nonlinear Finite Element Analysis* (pp. 367-426). Springer US : Imprint: Springer.

Knott, M., & Winters, M. (2018, 2018). *Ship and barge collisions with bridges over navigable waterways* [Conference paper]. PIANC-World Congress Panama City, Panama City. https://conference-service.com/pianc-panama/documents/agenda/data/full_papers/full_paper_46.pdf

Kristiansen, S. (2005). *Maritime transportation: safety management and risk analysis*. Elsevier/Butterworth-Heinemann.

Larsen, O. D. (1993). *Ship collision with bridges: The interaction between vessel traffic and bridge structures* (Vol. 4). IABSE. https://doi.org/10.2749/sed004

Li, Z. (2011). *Advanced concrete technology*. Wiley.

Lin, W., & Yoda, T. (2017). Steel Bridges. In W. Lin & T. Yoda (Eds.), *Bridge Engineering* (pp. 111-136). Butterworth-Heinemann. https://doi.org/https://doi.org/10.1016/B978-0-12-804432-2.00007-4

Liu, G. R., & Quek, S. S. (2013). *The Finite Element Method: A Practical Course*. Oxford: Elsevier Science & Technology.

LSTC. (2006). LS-DYNA Theoretical Manual. In (Vol. 05.03). 7374 Las Positas Road Livermore, California: Livermore Software Technology Corporation.

LSTC. (2021a). LS-DYNA KEYWORD USER'S MANUAL VOLUME 1. In (Vol. 2022). 7374 Las Positas Road Livermore, California 94551: Livermore Software Technology Corporation.

LSTC. (2021b). LS-DYNA KEYWORD USER'S MANUAL VOLUME II Material Models. In (Vol. 2022). 7374 Las Positas Road Livermore, California: Livermore Software Technology Corporation.

LSTC. (n.d.-a). *Contact modeling in LS-DYNA*. Livermore Software Technology Corporation. Retrieved 07.03 from https://www.dynasupport.com/tutorial/ls-dyna-users-guide/contact-modeling-in-ls-dyna

LSTC. (n.d.-b). *Elements*. Livermore Software Technology Corporation. Retrieved 14.03 from https://www.dynasupport.com/tutorial/ls-dyna-users-guide/elements

LSTC. (n.d.-c). *Hourglass*. Retrieved 20.04 from https://www.dynasupport.com/howtos/element/hourglass

LSTC. (n.d.-d). *Hourglass modes*. Livermore Software Technology Corporation. Retrieved 13.06 from https://ftp.lstc.com/anonymous/outgoing/support/FAQ_docs/hourglass.pdf

LSTC. (n.d.-e). *LS-DYNA*. Livermore Software Technology Corporation. Retrieved 03.04 from https://www.lstc.com/products/ls-dyna

LSTC. (n.d.-f). *LS-Prepost*. Livermore Software Technology Corporation. Retrieved 07.03 from https://www.lstc.com/products/ls-prepost

LSTC. (n.d.-g). *Time integration*. Livermore Software Technology Corporation. Retrieved 07.03 from https://www.dynasupport.com/tutorial/ls-dyna-users-guide/time-integration

LSTC. (n.d.-h). *Total energy*. Livermore Software Technology Corporation. Retrieved 04.05 from https://www.dynasupport.com/howtos/general/total-energy

Lutzen, M. (2001). *Ship collision damage* Technical University of Denmark]. https://core.ac.uk/download/pdf/13745655.pdf

Mehreganian, N., Louca, L. A., Langdon, G. S., Curry, R. J., & Abdul-Karim, N. (2018). The response of mild steel and armour steel plates to localised air-blast loading-comparison of numerical modelling techniques. *International journal of impact engineering*, *115*, 81-93. https://doi.org/10.1016/j.ijimpeng.2018.01.010

Mesquita, D. (2021). *Python AI: How to Build a Neural Network & Make Predictions*. Realpython. Retrieved 08.05 from https://realpython.com/python-ai-neural-network/

Minorsky, V. U. (1958). *An analysis of ship collisions with reference to protection of nuclear power plants*.

Neto, M. A., Amaro, A., Roseiro, L., Cirne, J., & Leal, R. (2015). *Engineering Computation of Structures: The Finite Element Method* (1st 2015 ed.). Cham: Springer International Publishing. https://doi.org/10.1007/978-3-319-17710-6

Nikishkov, G. P. (2009). INTRODUCTION TO THE FINITE ELEMENT METHOD. *Lecture Notes. University of Aizu, Aizu-Wakamatsu 965-8580, Japan*, 5.

NORSOK. (2013). *N-004 Design of steel structures* (NORSOK standard, Issue. https://www-standard-no.ezproxy.uis.no/pagefiles/1145/n-004.pdf

Oasis. (2018). Introduction to LS-DYNA MPP. https://www.oasys-software.com/dyna/wp-content/uploads/2019/01/Webinar_MPP-LS-DYNA.pdf

Oxford. (n.d.). Risk. In *Oxford Advanced Learner's Dictionary*: Oxford University Press.

Pedersen, P. T., Chen, J., & Zhu, L. (2020). Design of bridges against ship collisions. *Marine Structures*, *74*, 102810.

Pedersen, P. T., Valsgaard, S., Olsen, D., & Spangenberg, S. (1993). Ship impacts: bow collisions. *International Journal of Impact Engineering*, *13*(2), 163-187.

Rao, S. S. (2018). *Mechanical vibrations* (6th in SI units, Global ed.). Pearson Education.

Sha, Y., & Hao, H. (2012). Nonlinear finite element analysis of barge collision with a single bridge pier. *Engineering Structures*, *41*, 63–76. https://doi.org/10.1016/j.engstruct.2012.03.026

Sha, Y., & Hao, H. (2013). Numerical simulation of barge impact on a continuous girder bridge and bridge damage detection. *International Journal of Protective Structures*, *4*(1), 79-96.

Sha, Y., & Hao, H. (2014). A simplified approach for predicting bridge pier responses subjected to barge impact loading. *Advances in Structural Engineering*, *17*(1), 11-23.

Tran, N. K., & Haasis, H.-D. (2015). An empirical study of fleet expansion and growth of ship size in container liner shipping. *International journal of production economics*, *159*, 241-253. https://doi.org/10.1016/j.ijpe.2014.09.016

Wang, Z., Dueñas-Osorio, L., & Padgett, J. E. (2014). Influence of scour effects on the seismic response of reinforced concrete bridges. *Engineering structures*, *76*, 202-214. https://doi.org/10.1016/j.engstruct.2014.06.026

Woisin, G. (1976). The collision tests of the GKSS. *Jahrbuch der Schiffbautechnischen Gesellschaft*, *70*(2), 465-487.

Yuan, P., & Harik, I. E. (2008). One-dimensional model for multi-barge flotillas impacting bridge piers. *Computer-Aided Civil and Infrastructure Engineering*, *23*(6), 437-447.

Zhang, S., Pedersen, P. T., & Villavicencio, R. (2019a). External dynamics of ship collisions and grounding. In S. Zhang, P. T. Pedersen, & R. Villavicencio (Eds.), *Probability and Mechanics of Ship Collision and Grounding* (pp. 62-146). Butterworth-Heinemann. https://doi.org/10.1016/B978-0-12-815022-1.00002-5

Zhang, S., Pedersen, P. T., & Villavicencio, R. (2019b). Internal mechanics of ship collision and grounding. In S. Zhang, P. T. Pedersen, & R. Villavicencio (Eds.), *Probability and Mechanics of Ship Collision and Grounding* (pp. 147-270). Butterworth-Heinemann. https://doi.org/10.1016/B978-0-12-815022-1.00003-7

Zhang, S., Pedersen, P. T., & Villavicencio, R. (2019c). Probability of ship collision and grounding. In S. Zhang, P. T. Pedersen, & R. Villavicencio (Eds.), *Probability and Mechanics of Ship Collision and Grounding* (pp. 1-61). Butterworth-Heinemann. https://doi.org/10.1016/B978-0-12-815022-1.00001-3

Zhou, Z.-H. (2021). *Machine Learning*. Springer Singapore. https://doi.org/10.1007/978-981-15-1967-3

Appendices

Appendix I: Python scripts for determining the collapse probability

Script 1

```
import numpy as np
import matplotlib.pyplot as plt
class NeuralNetwork:
    def __init__(self, learning_rate):
        self.weights = np.array([np.random.randn(), np.random.randn()])
        self.bias = np.random.randn()
        self.learning_rate = learning_rate

    def _sigmoid(self, x):
        return 1 / (1 + np.exp(-x))

    def _sigmoid_deriv(self, x):
        return self._sigmoid(x) * (1 - self._sigmoid(x))

    def predict(self, input_vector):
        layer_1 = np.dot(input_vector, self.weights) + self.bias
        layer_2 = self._sigmoid(layer_1)
        prediction = layer_2
        return prediction

    def _compute_gradients(self, input_vector, target):
        layer_1 = np.dot(input_vector, self.weights) + self.bias
        layer_2 = self._sigmoid(layer_1)
        prediction = layer_2

        derror_dprediction = 2 * (prediction - target)
        dprediction_dlayer1 = self._sigmoid_deriv(layer_1)
        dlayer1_dbias = 1
        dlayer1_dweights = (0 * self.weights) + (1 * input_vector)

        derror_dbias = (
            derror_dprediction * dprediction_dlayer1 * dlayer1_dbias
        )
        derror_dweights = (
            derror_dprediction * dprediction_dlayer1 * dlayer1_dweights
        )

        return derror_dbias, derror_dweights
```

```
    def _update_parameters(self, derror_dbias, derror_dweights):
        self.bias = self.bias - (derror_dbias * self.learning_rate)
        self.weights = self.weights - (
            derror_dweights * self.learning_rate
        )

    def train(self, input_vectors, targets, iterations):
        cumulative_errors = []
        for current_iteration in range(iterations):
            # Pick a data instance at random
            random_data_index = np.random.randint(len(input_vectors))

            input_vector = input_vectors[random_data_index]
            target = targets[random_data_index]

            # Compute the gradients and update the weights
            derror_dbias, derror_dweights = self._compute_gradients(
                input_vector, target
            )

            self._update_parameters(derror_dbias, derror_dweights)

            # Measure the cumulative error for all the instances
            if current_iteration % 100 == 0:
                cumulative_error = 0
                # Loop through all the instances to measure the error
                for data_instance_index in range(len(input_vectors)):
                    data_point = input_vectors[data_instance_index]
                    target = targets[data_instance_index]

                    prediction = self.predict(data_point)
                    error = np.square(prediction - target)

                    cumulative_error = cumulative_error + error
                cumulative_errors.append(cumulative_error)
        return cumulative_errors

learning_rate = 0.1
neural_network = NeuralNetwork(learning_rate)

velocity_mass = np.array([[3, 1], [3, 2], [3, 3], [3, 4],
                          [4, 1], [4, 2], [4, 3], [4, 4],
                          [5, 1], [5, 2], [5, 3], [5, 4]])
```

```
velocity_mass_target = np.array([0, 0, 0, 0,
                                 0, 0, 0, 1,
                                 0, 0, 1, 1])


velocity_mass_training_error = neural_network.train(velocity_mass,
velocity_mass_target, 100000)

velocity_mass_prediction = neural_network.predict([int(input("Enter velocity (in
m/s):")),int(input("Enter mass (in thousand tons):"))])


print(velocity_mass_prediction)

plt.plot(velocity_mass_training_error)
plt.xlabel("number of iterations")
plt.ylabel("error")
plt.savefig("vel_mass_training_error.png")
plt.show()
```

Script 2

```
import numpy as np
import matplotlib.pyplot as plt
class NeuralNetwork:
    def __init__(self, learning_rate):
        self.weights = np.array([np.random.randn(), np.random.randn()])
        self.bias = np.random.randn()
        self.learning_rate = learning_rate

    def _sigmoid(self, x):
        return 1 / (1 + np.exp(-x))

    def _sigmoid_deriv(self, x):
        return self._sigmoid(x) * (1 - self._sigmoid(x))

    def predict(self, input_vector):
        layer_1 = np.dot(input_vector, self.weights) + self.bias
        layer_2 = self._sigmoid(layer_1)
        prediction = layer_2
        return prediction

    def _compute_gradients(self, input_vector, target):
        layer_1 = np.dot(input_vector, self.weights) + self.bias
        layer_2 = self._sigmoid(layer_1)
        prediction = layer_2

        derror_dprediction = 2 * (prediction - target)
        dprediction_dlayer1 = self._sigmoid_deriv(layer_1)
        dlayer1_dbias = 1
        dlayer1_dweights = (0 * self.weights) + (1 * input_vector)

        derror_dbias = (
            derror_dprediction * dprediction_dlayer1 * dlayer1_dbias
        )
        derror_dweights = (
            derror_dprediction * dprediction_dlayer1 * dlayer1_dweights
        )

        return derror_dbias, derror_dweights

    def _update_parameters(self, derror_dbias, derror_dweights):
        self.bias = self.bias - (derror_dbias * self.learning_rate)
        self.weights = self.weights - (
            derror_dweights * self.learning_rate
```

```
        )

    def train(self, input_vectors, targets, iterations):
        cumulative_errors = []
        for current_iteration in range(iterations):
            # Pick a data instance at random
            random_data_index = np.random.randint(len(input_vectors))

            input_vector = input_vectors[random_data_index]
            target = targets[random_data_index]

            # Compute the gradients and update the weights
            derror_dbias, derror_dweights = self._compute_gradients(
                input_vector, target
            )

            self._update_parameters(derror_dbias, derror_dweights)

            # Measure the cumulative error for all the instances
            if current_iteration % 100 == 0:
                cumulative_error = 0
                # Loop through all the instances to measure the error
                for data_instance_index in range(len(input_vectors)):
                    data_point = input_vectors[data_instance_index]
                    target = targets[data_instance_index]

                    prediction = self.predict(data_point)
                    error = np.square(prediction - target)

                    cumulative_error = cumulative_error + error
                cumulative_errors.append(cumulative_error)
        return cumulative_errors

learning_rate = 0.1
neural_network = NeuralNetwork(learning_rate)

KE_angle = np.array     ([[24, 0], [24, 15], [24, 30], [24, 45], [24, 60], [24,
90],
                          [32, 0], [32, 15], [32, 30], [24, 45], [32, 60], [32,
90],
                          [37.5, 0], [37.5, 15], [24, 60], [37.5, 45], [37.5,
60], [37.5, 90],
                          [50, 0], [50, 15], [50, 30], [24, 45], [50, 60], [50,
90]])
```

```
KE_angle_target = np.array     ([0, 0, 0, 0, 0, 0,
                                  1, 1, 1, 1, 0, 0,
                                  1, 1, 1, 0, 0, 0,
                                  1, 1, 1, 1, 1, 1])

KE_angle_training_error = neural_network.train(KE_angle, KE_angle_target, 100000)

KE_angle_prediction = neural_network.predict([int(input("Enter KE (in
MJ):")),int(input("Enter angle of impact (in degrees):"))])


print(KE_angle_prediction)

plt.plot(KE_angle_training_error)
plt.xlabel("number of iterations")
plt.ylabel("error")
plt.savefig("KE_angle_training_error.png")
plt.show()
```

Appendix II: Calculation of spring forces

Properties and coefficients

Dry sand density	ρ_{sand}	19	kN/m^3
soil friction angle		33	%
Relative density		50	%
Water density	ρ_{water}	9.8	kN/m^3
Effective soil weight	ρ_{eff}	9.2	kN/m^3
Clearance below bridge		15.9	m
Depth of water layer		16	m
Depth of sand layer		23.9	m
Pile diameter	D	0.5	m
Pile depth	H	22.3	m
Side surface area of pile	As	35.02875809	m2
Gross end area of pile	Ap	0.196349541	m2
maximum effective overpressure	p'_0	376.68	kPa
Dimensionless shaft friction factor	β	0.37	
Dimensionless bearing capacity factor	N_q	20	
Maximum unit shaft friction	f	139.3716	kPa
Unit end bearing	q	7533.6	kPa
Limiting shaft friction values	f_{max}	81	kPa
Limiting unit end bearing values	q_{max}	5000	kpa
Unit soil pile adhesion	t_{max}	81	kPa
Total end bearing	Q_p	981.7477042	kN

Lateral bearing capacity factors	
C1	2.5
C2	3.3
C3	45

T-z load curves

z (in)	t/tmax (lb/ft2)
0.0000	0.0000
0.1000	1.0000
∞	1.0000

=>

z (m)	t/tmax (Kpa)
0.0000	0.0000
0.0025	1.0000
∞	1.0000

=>

z (m)	t (kPa)
0.0000	0.0000
0.0025	81.0000
0.1000	81.0000

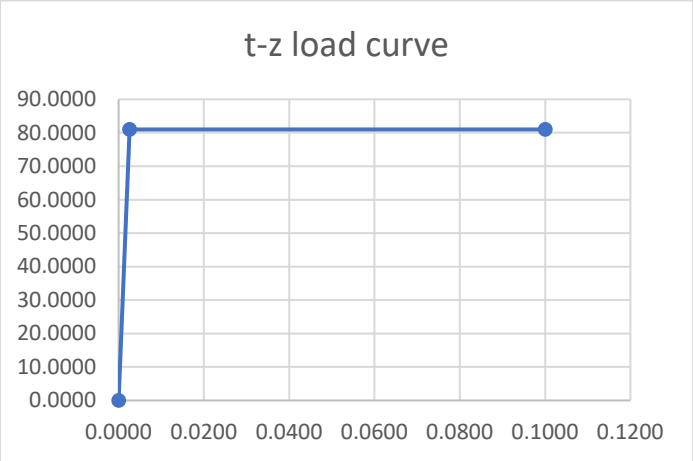

Q-z load curve

z/D (in)	Q/Qp (lb)
0.0020	0.2500
0.0130	0.5000
0.0420	0.7500
0.0730	0.9000
0.1000	1.0000

=>

z (in)	Q (lb)
0.0394	55176.6753
0.2559	110353.3507
0.8268	165530.0260
1.4370	198636.0313
1.9685	220706.7014

=>

z (m)	Q (kN)
0.0000	0.0000
0.0010	245.4259
0.0065	490.8517
0.0210	736.2776
0.0365	883.5331
0.0500	981.7034
0.1000	981.7034

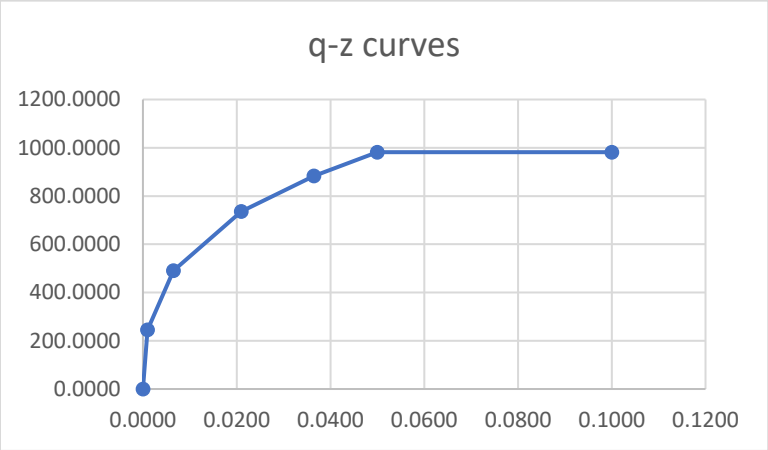

P-y load curves

	A	0.9	(assumed for z=H/2)
ultimate bearing capacity	pu	4616.1	kN/m
Initial modulus of subgrade reaction	k	60	lb/in3
Initial modulus of subgrade reaction	k	16680.84	kN/m3

z (m)	P (kN/m)
0	0
0.0010	185.8668
0.0065	1175.9351
0.0210	3054.7447
0.0365	3849.7046
0.0500	4061.0873
0.1000	4153.4162

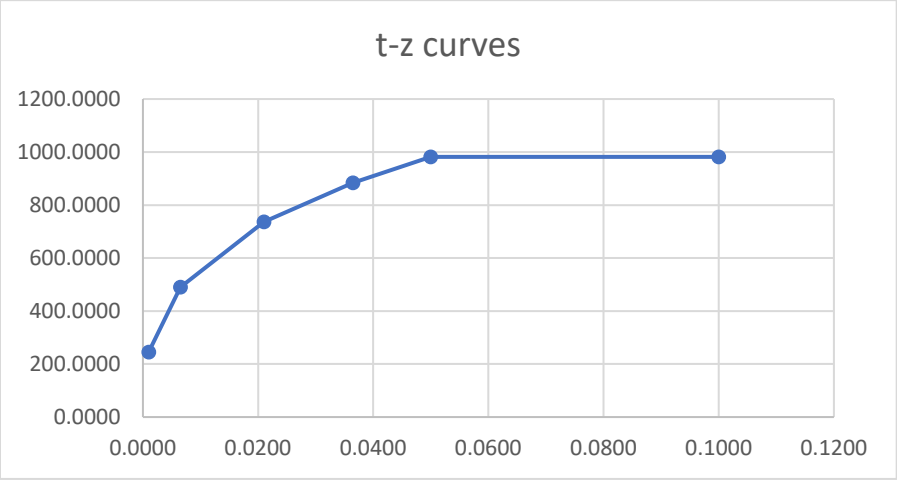

Pile group effect for p-y springs

	Row 1	Row 2	Row 3
P-multiplier	1	0.85	0.7

Row 1	
z (m)	P (kN/m)
0.0000	0.0000
0.0010	185.8668
0.0065	1175.9351
0.0210	3054.7447
0.0365	3849.7046
0.0500	4061.0873
0.1000	4153.4162

Row 2	
z (m)	P (kN/m)
0.0000	0.0000
0.0010	157.9868
0.0065	999.5448
0.0210	2596.5330
0.0365	3272.2489
0.0500	3451.9242
0.1000	3530.4038

Row 3	
z (m)	P (kN/m)
0.0000	0.0000
0.0010	130.1068
0.0065	823.1545
0.0210	2138.3213
0.0365	2694.7932
0.0500	2842.7611
0.1000	2907.3913

Spring forces

Amount of spring sets	23

Pile diameter	D	0.5	m
Pile depth	H	23.9	m
Side surface area of pile	As	37.542	m2
Gross end area of pile	Ap	0.196	m2

t-z curve	
z (m)	t (kPa)
0.0000	0.0000
0.0025	81.0000
0.1000	81.0000

=>

Force on each t-z spring	
z (m)	F (kN)
0.0000	0.0000
0.0254	132.2132
0.1000	132.2132

q-z curve	
z (m)	Q (kN)
0.0000	0.0000
0.0010	245.4259
0.0065	490.8517
0.0210	736.2776
0.0365	883.5331
0.0500	981.7034
0.1000	981.7034

=>

Force on each q-z spring	
z (m)	Q (kN)
0.0000	0.0000
0.0010	245.4259
0.0065	490.8517
0.0210	736.2776
0.0365	883.5331
0.0500	981.7034
0.1000	981.7034

p-y curve	
z (m)	P (kN/m)
0.0000	0.0000
0.0010	185.8668
0.0065	1175.9351
0.0210	3054.7447
0.0365	3849.7046
0.0500	4061.0873
0.1000	4153.4162

=>

Force on each p-y spring	
z (m)	F (kN)
0.00	0.00
0.00	193.14
0.01	1221.95
0.02	3174.28
0.04	4000.35
0.05	4220.00
0.10	4315.94

Row 1

p-y curve	
z (m)	P (kN/m)
0	0
0.0010	185.8668
0.0065	1175.9351
0.0210	3054.7447
0.0365	3849.7046
0.0500	4061.0873
0.1000	4153.4162

=>

Force on each p-y spring	
z (m)	F (kN)
0.00	0.00
0.00	193.14
0.01	1221.95
0.02	3174.28
0.04	4000.35
0.05	4220.00
0.10	4315.94

Row 2

p-y curve	
z (m)	P (kN/m)
0.0000	0.0000
0.0010	157.9868
0.0065	999.5448
0.0210	2596.5330
0.0365	3272.2489
0.0500	3451.9242
0.1000	3530.4038

=>

Force on each p-y spring	
z (m)	F (kN)
0.00	0.00
0.00	164.17
0.01	1038.66
0.02	2698.14
0.04	3400.29
0.05	3587.00
0.10	3668.55

Row 3

p-y curve	
z (m)	P (kN/m)
0.0000	0.0000
0.0010	130.1068
0.0065	823.1545
0.0210	2138.3213
0.0365	2694.7932
0.0500	2842.7611
0.1000	2907.3913

=>

Force on each p-y spring	
z (m)	F (kN)
0.00	0.00
0.00	135.20
0.01	855.36
0.02	2221.99
0.04	2800.24
0.05	2954.00
0.10	3021.16